

## Title page

### Title

OMSV enables accurate and comprehensive identification of large structural variations from nanochannel-based single-molecule optical maps

### Authors

Le Li<sup>1,\*</sup> (lil@cse.cuhk.edu.hk), Alden King-Yung Leung<sup>2,\*</sup> (alden.leung@gmail.com), Tsz-Piu Kwok<sup>1,\*</sup> (kwoktszpiu@gmail.com), Yvonne Y.Y. Lai<sup>3</sup> (lyvonne0912@gmail.com), Iris K. Pang<sup>2</sup> (irisipang@cuhk.edu.hk), Grace Tin-Yun Chung<sup>4</sup> (gracechung@cuhk.edu.hk), Angel C.Y. Mak<sup>3</sup> (maka@humgen.ucsf.edu), Annie Poon<sup>3</sup> (annie.poon@ucsf.edu), Catherine Chu<sup>3</sup> (catherine.chu@ucsf.edu), Menglu Li<sup>5</sup> (mlli@cs.hku.hk), Jacob J.K. Wu<sup>5</sup> (jacobwu@braininvesting.com), Ernest T. Lam<sup>6</sup> (elam@bionanogenomics.com), Han Cao<sup>6</sup> (han@bionanogenomics.com), Chin Lin<sup>3</sup> (chinlin2004@yahoo.com), Justin Sibert<sup>7</sup> (justin.sibert@gmail.com), Siu-Ming Yiu<sup>5</sup> (smyiu@cs.hku.hk), Ming Xiao<sup>7</sup> (mx44@drexel.edu), Kwok-Wai Lo<sup>4</sup> (kwlo@cuhk.edu.hk), Pui-Yan Kwok<sup>3,8</sup> (pui.kwok@ucsf.edu), Ting-Fung Chan<sup>2,9,10,11,†</sup> (tf.chan@cuhk.edu.hk) and Kevin Y. Yip<sup>1,9,10,11,†</sup> (kevinyip@cse.cuhk.edu.hk)

### Addresses

<sup>1</sup>Department of Computer Science and Engineering, <sup>2</sup>School of Life Sciences, The Chinese University of Hong Kong, Shatin, New Territories, Hong Kong

<sup>3</sup>Cardiovascular Research Institute, University of California San Francisco, San Francisco, California, USA

<sup>4</sup>Department of Anatomical and Cellular Pathology, The Chinese University of Hong Kong, Shatin, New Territories, Hong Kong

<sup>5</sup>Department of Computer Science, The University of Hong Kong, Hong Kong

<sup>6</sup>BioNano Genomics, San Diego, California, USA

<sup>7</sup>School of Biomedical Engineering, Science and Health Systems, Drexel University, Philadelphia, Pennsylvania, USA

<sup>8</sup>Institute for Human Genetics, University of California San Francisco, San Francisco, California, USA

<sup>9</sup>Hong Kong Bioinformatics Centre, <sup>10</sup>Hong Kong Institute of Diabetes and Obesity, <sup>11</sup>CUHK-BGI Innovation Institute of Trans-omics, The Chinese University of Hong Kong, Shatin, New Territories, Hong Kong

\*Co-first authors †Co-corresponding authors



## METHOD

# OMSV enables accurate and comprehensive identification of large structural variations from nanochannel-based single-molecule optical maps

Le Li<sup>1\*</sup>, Alden King-Yung Leung<sup>2\*</sup>, Tsz-Piu Kwok<sup>1\*</sup>, Yvonne Y.Y. Lai<sup>3</sup>, Iris K. Pang<sup>2</sup>, Grace Tin-Yun Chung<sup>4</sup>, Angel C.Y. Mak<sup>3</sup>, Annie Poon<sup>3</sup>, Catherine Chu<sup>3</sup>, Menglu Li<sup>5</sup>, Jacob J.K. Wu<sup>5</sup>, Ernest T. Lam<sup>6</sup>, Han Cao<sup>6</sup>, Chin Lin<sup>3</sup>, Justin Sibert<sup>7</sup>, Siu-Ming Yiu<sup>5</sup>, Ming Xiao<sup>7</sup>, Kwok-Wai Lo<sup>4</sup>, Pui-Yan Kwok<sup>3,8</sup>, Ting-Fung Chan<sup>2,9,10,11†</sup> and Kevin Y. Yip<sup>1,9,10,11†</sup>

## Abstract

We present a new method, OMSV, for accurately and comprehensively identifying structural variations (SVs) from optical maps. OMSV detects both homozygous and heterozygous SVs, SVs of various types and sizes, and SVs with or without creating/destroying restriction sites. We show that OMSV has high sensitivity and specificity, with clear performance gains over the latest existing method. Applying OMSV to a human cell line, we identified hundreds of SVs >2kbp, with 68% of them missed by sequencing-based callers. Independent experimental validations confirmed the high accuracy of these SVs. The OMSV software is available at <http://yiplab.cse.cuhk.edu.hk/omsv/>.

**Keywords:** optical mapping; nanochannel; single-molecule analysis; structural variation

## Background

Structural variations (SVs), defined as genomic alterations involving segments larger than 1kbp [1], are prevalent in human genomes. They represent characteristic differences among human populations [2], and are associated with various diseases [3, 4].

Current sequencing technologies, including second-generation and commercial third-generation sequencing platforms, produce sequencing reads from a hundred to tens of thousands of base pairs only, making it challenging to study long repetitive regions and complex structural rearrangements. For instance, some large insertions cannot be contained in a single read, and their detection requires either sequence assembly [5] or reference alignment [6, 7], with the help of paired-end or mate-pair sequencing with large insert sizes [8, 9]. In general, these methods are not ideal for detecting large SVs accurately and comprehensively, especially SVs that involve long DNA sequences not present in the reference sequence [10, 11].

Optical mapping (OM) [12] is a promising alternative technology that provides structural information of

individual long DNA molecules. In nanochannel-based optical mapping [13, 14], DNA molecules are digested by a nicking endonuclease to create single-strand nicks, which are then repaired with fluorescent dye conjugated nucleotides. The resulting DNA molecules are linearized in nanochannels and imaged using high-resolution fluorescent microscopy (Additional file 1: Figure S1). The final outputs are the optical maps, which record restriction site label locations on each DNA molecule. SVs can be identified by comparing the observed label pattern with the expected pattern based on the reference sequence (Figure 1a). For example, two sites significantly farther apart on an optical map than their corresponding locations on the reference could indicate an insertion.

Due to the much longer length of optical maps (up to 1Mbp) compared to sequencing reads, OM has been found very powerful in SV discovery [13, 15–18]. Current high-throughput OM methods can produce optical maps for a hundred thousand molecules within a few hours, at an average size of several hundred kbps per molecule. These molecules can be full-length DNA derived from species with a small genome, or fragments of very long DNA molecules such as human chromosomes.

Full list of author information is available at the end of the article

\*Co-first authors with equal contribution.

†Correspondence: KY Yip(kevinyip@cse.cuhk.edu.hk) and TF Chan(tf.chan@cuhk.edu.hk)

Analyzing optical maps is non-trivial due to various types of error present in the data [19, 20]. False positives (false labels observed but not coming from true restriction sites) can occur due to non-specific enzymatic cuts or DNA breakage. False negatives (true restriction sites not observed on the optical maps) can occur due to incomplete enzyme digestion. Sizing errors (deviation between measured and actual distance between two restriction sites on an optical map) can occur due to DNA fragments that are over-stretched or not completely linearized. Finally, labels of close restriction sites may merge into a single label in the observed data due to limitations in imaging resolution. As a result of all these error types, specialized methods have been proposed for various computational tasks related to the analysis of optical maps, including error modeling [19, 21], molecule alignment [18, 20, 22–24], *de novo* and reference-assisted assembly [20, 25, 26], and detection of SVs [13, 17, 18, 27].

Existing methods for calling SVs from optical maps have several major limitations (Additional file 1: Table S1). First, most of them require a *de novo* assembly of the optical maps or the construction of a consensus map [13, 15, 18], making the accuracy of SV calls dependent on the reliability of these difficult procedures. Second, none of the current methods can simultaneously 1) detect both homozygous and heterozygous SVs, 2) handle SVs of a wide range of sizes, and 3) evaluate SV probabilities based on a formal error model and the optical maps that support/do not support the SVs. Besides, almost none of the existing methods have made their software publicly available, which hampers the widespread use of optical mapping in studying SVs.

Here we describe a comprehensive SV calling pipeline and corresponding open-source software, OMSV (available at the supplementary Web site, <http://yiplab.cse.cuhk.edu.hk/omsv/>, under the MIT license), which overcomes these limitations. We demonstrate the effectiveness of OMSV using both simulations and optical maps produced from a family trio. In addition, we show that when OMSV was applied to detect SVs in a human cell line, many of our detected SVs were missed by typical sequencing-based SV callers. Some of our detected SVs were experimentally tested using DNA isolated from the cell line, and most of them were successfully validated. Finally, we describe how OMSV can combine optical maps and sequencing data to identify precise SV break points and uncover novel sequences involved in the SVs.

## Results

### The OMSV pipeline

OMSV contains two main steps (Figure 1b, Methods). In the first step, it aligns optical maps to the reference

map, which is deduced from the reference sequence and the recognition motif of the nicking enzyme by *in silico* digestion. Two different aligners are used, namely ReAligner [24], which can efficiently align optical maps highly similar to the reference, and OMBlast [22], which can handle more complex genomic rearrangements by split-aligning a single optical map to multiple regions on the reference. The alignment results from the two aligners are integrated to form a single set of consensus alignments. In the second step of OMSV, these alignments are passed to three separate SV calling modules for three corresponding types of SVs, which are 1) SVs involving the creation or removal of restriction sites, 2) SVs involving large distance changes between restriction sites, and 3) more complex SVs such as inversions and translocations. SVs identified from these modules are then integrated and de-duplicated to form a final list of SVs.

In the SV calling modules, a formal error model is used to compare the likelihoods of the reference genotype (i.e., no SVs), homozygous SVs, and heterozygous SVs. An SV is called only if a set of stringent criteria are satisfied (Figure 2, Methods).

### Simulations confirm the effectiveness of OMSV

To test the effectiveness of OMSV, we generated simulated OM data from artificial haploid and diploid human genomes, by introducing various types of genetic variants to the reference genome hg38 followed by simulation of noisy optical maps with all types of error (Methods). We defined a default error setting, and additional settings that covered a wide range of false positive and false negative rates of nicking sites and depths of coverage, leading to a total of 28 sets of simulated OM data (Additional file 1: Tables S2,S3). In the original paper that describes the nanochannel-based optical mapping method [13], the false positive and false negative rates were reported to be 21% and 4%, respectively. According to our experience, the current systems have around 10% false negative labels and 1 false positive label per 100kbp. In the default error setting, we set these parameters to slightly higher values to test OMSV's ability to handle noisy data (Additional file 1: Table S2).

Next, we applied OMSV to identify SVs from these simulated OM data sets, and compared the results to the actual lists of synthesized SVs in order to determine OMSV's precision (fraction of called SVs that are correct) and recall (fraction of simulated SVs correctly called by OMSV).

Here we first focus on insertions and deletions (indels) larger than 2kbp in the data sets with the default setting, since they constitute a large fraction of our simulated SVs and these large SVs are difficult for

short-read based methods to identify accurately. In the case of the haploid genome, both the precision and recall of OMSV were 98% for deletions and 95% for insertions (Figures 3a,b), showing that it was highly effective. In the case of the diploid genome, when the goal was to identify SV locations only without considering correctness of zygosity, OMSV again achieved high precision (99%) and recall (92%) for deletions, and high precision (97%) and moderate recall (81%) for insertions due to fewer optical maps supporting the SVs in the heterozygous cases. When correct zygosity was also required for an SV to be considered correctly called, OMSV still achieved 90% precision and 81% recall on average. For the SVs correctly identified from the two data sets, we further compared their estimated sizes by OMSV with the actual sizes up to the closest defining nicking sites, and found them to be very similar in most cases (Figures 3c,d), with a median size ratio of 1.0028 and 1.0029 for the haploid and diploid data sets, respectively.

To benchmark the performance of OMSV, we compared it with the latest version of the assembly-based SV caller BioNano Solve, which is the only other SV caller for nanochannel-based optical mapping with publicly available software (the SV caller used in Cao et al. [15] is a previous version of this software). We found that the precision of the two methods was comparable, but OMSV had 10%-31% higher recall (Figures 3e,f). Moreover, since BioNano Solve required a *de novo* assembly of the optical maps, its running time was 16-21 times longer than OMSV (including the alignment time).

To evaluate the robustness of OMSV, we performed three additional sets of tests. First, using the diploid data set with default settings, we checked the SVs with various numbers of optical maps aligned to their loci and having different likelihood ratios as computed by OMSV. We found that OMSV's precision remained highly stable at different values of these variables (Additional file 1: Figure S2), and the default parameter values of OMSV (at least 10 aligned optical maps and a null-to-alternative likelihood ratio of at most  $10^{-6}$  for an SV to be called) provided a good tradeoff between precision and recall. Second, we compared the performance of OMSV on data sets with different depths of coverage. To separate the effects of alignment errors and SV calling errors, we also considered an idealized situation with no alignment errors (Methods). The depth of coverage was found to have virtually no effects on the precision of OMSV for the depth values considered (Additional file 1: Figure S3a), but it correlated with the recall (Additional file 1: Figure S3b), with almost no SVs being called when the coverage went down to around 5x. Importantly, by comparing

our results with and without involving optical map alignments, we found that the decreased recall at low depth of coverage was largely due to alignment errors as seen by the big drop of recall with the actual alignment as compared to the case with perfect alignment at the same data coverage. Third, we altered the false positive and false negative rates of the OM data, and found that the performance of OMSV remained stable for most settings until the error rates reached unrealistically large values not typically seen in real data (Additional file 1: Figures S4,S5). Again, we found that the performance drop at high false positive and false negative rates correlated strongly with alignment errors, and thus the performance of OMSV should be automatically improved with better alignment accuracy. Overall, these three sets of tests show that OMSV is generally robust against different data properties and parameter settings.

We also compared different alignment strategies involving alignments from only one of the two aligners, their intersection, and their union. The results (Additional file 1: Figure S6) show that taking the union of the two aligners had the best tradeoff between precision and recall, especially when the data set had a low depth of coverage.

For complex SVs (Figures 3g,h), OMSV achieved 80-85% precision but only 30-50% recall on the two default sets. Many of the missed SVs were found to be intrinsically infeasible to call, including inversions that contain no nicking sites or symmetric nicking site patterns that would not change upon the inversions. After filtering these cases, the recall rate of the resulting intrinsically feasible (IF) complex SVs was substantially improved to 45-80%. BioNano Solve contained a function for calling complex SVs, but failed to detect any of them from the simulated data.

Taken together, the simulation results show that OMSV can identify large SVs accurately and comprehensively on data sets with properties typical in real data.

In terms of running time of OMSV, the main bottleneck was optical map alignments (Additional file 1: Table S4). This limitation can be overcome by running the aligners on multiple threads in parallel, leading to an overall running time of OMSV of less than 5 hours for each simulated human sample with a 100x genome coverage.

#### OMSV identifies SVs concordantly from different members of a family

We next tested OMSV on the optical maps produced from a family trio in a former study [28] (Additional file 1: Table S5). Genetic variants from this trio were previously reported [29], but they are mostly small

variants. OMSV called 1,054–1,126 large indels from the three samples independently (Additional file 1: Table S6, Additional file 2, Methods), with an average size of 6.4kbp and a maximum of 89kbp. In addition, there were 22 other loci with two indels called at the same locus. OMSV also called 86–158 complex SVs from the three individuals in this trio. Since the actual SVs in these individuals were not known, we used four different methods to estimate the accuracy of OMSV.

First, we hid the sex of the samples from OMSV, and checked the number of SV calling errors related to the sex chromosomes (Additional file 1: Table S6). When pseudo-autosomal regions were excluded, in the female samples NA12878 and NA12892, 59 and 55 SVs were called on the X chromosome, respectively, whereas no SVs were wrongly called on the Y chromosome. In terms of zygosity, the male sample NA12891 had 18 indels wrongly called as heterozygous among the 53 indels called on the non-pseudo-autosomal regions of the sex chromosomes. Based on these numbers, the estimated zygosity precision was  $(53-18)/53 = 66\%$ .

Second, we compared the indels called from the three individuals. Among the high-confidence calls (Methods), 99% were concordant with Mendelian inheritance when zygosity of the SVs was ignored, and 86% were concordant when zygosity was considered. We used the precision and recall values from our simulations to estimate the expected Mendelian concordance to be 96% when zygosity was ignored and 83% when zygosity was considered (Methods), suggesting that the accuracy of OMSV on the trio data was comparable to that on the simulated data.

Third, we compared our SV calls with the manual checking results from Mak *et al.* [28] based on nicking site patterns of aligned molecules (Additional file 1: Table S7). Among our SVs with manual checking results, in the three individuals 96–97% of them were considered correct by the manual checking results when zygosity was ignored, which is similar to the precision values in the simulation study. When zygosity was considered, 73–74% of our SVs were considered correct by the manual checking results, which is lower than that in the simulation. Together, these results suggest that OMSV could identify SV locations accurately but determining the correct zygosity of the SVs could be more difficult with real data.

Finally, we compared our indel list from NA12878 with two lists of indels detected from this sample previously using sequencing-based methods [2, 30]. Focusing on large (>2kbp) indels, the intersection of OMSV's list and either of these two sequencing-based lists (81 and 90 indels, respectively) was similar to the intersection of these two lists (84 indels) (Additional file 1: Figure S7). Interestingly, 500 (96%) of the insertions

and 178 (38%) of the deletions called by OMSV were unique among the three lists. Based on the above estimation of the accuracy of OMSV, a large fraction of these novel indels are expected to be real. These observations suggest that OMSV is able to identify SVs commonly called by other sequencing-based methods as well as uncover novel ones missed by them.

We select two examples to illustrate the SVs identified by OMSV. In the first example on chromosome 6 (Figure 4a), the father (NA12891) has a heterozygous insertion of around 14.6kbp, the mother (NA12892) has a heterozygous insertion of around 22.7kbp, and the daughter (NA12878) inherits both insertions from the parents. This example demonstrates the abilities of OMSV in identifying heterozygous SVs and loci with two distinct alleles both different from the reference. In the second example (Figure 4b), a large inversion of around 123.3kbp was consistently found on chromosome X from all three individuals, with clear nicking site patterns that support the inversion.

#### OMSV identifies many SVs missed by short-read based SV callers

To further evaluate the ability of OMSV in detecting novel SVs, we produced optical maps from the human C666-1 cell line [31] (Additional file 1: Table S8). C666-1 cells consistently harbor multiple Epstein-Barr virus (EBV) episomes. As a first check of the data produced, we aligned the optical maps to the EBV reference in C666-1 [32], and found a large number of well-aligned optical maps (Additional file 1: Figure S8). Comparing the average depth of coverage of the optical maps aligned to the human (72x) and EBV (847x) references, we estimated an average of 24 copies of the EBV genome per C666-1 cell, which is highly consistent with a previous estimate based on sequencing data [33].

We then applied OMSV to identify SVs in the C666-1 cellular genome (Additional file 1: Table S9, Additional file 3). In total 810 loci containing indels larger than 2kbp were called, with an average size of 6.6kbp and a maximum of 106kbp. Among the large indels identified, 67% were insertions while 33% were deletions, and 69% were homozygous while 31% were heterozygous. Since C666-1 was originally derived from a male sample, we checked the number of indels wrongly called as heterozygous on the sex chromosomes (Additional file 1: Table S9), and found 6 such errors among the 21 (29%) SVs identified, which is close to the error rate we obtained from NA12891 (34%). To investigate the origin of our identified indels, we intersected them with segmental duplications in the human genome [34, 35]. We found 143 of the C666-1 large indels overlapping with segmental duplication regions, among which 78 involved segmental duplications that overlap exons of

protein coding genes (Additional file 4). Therefore at least 18% of the SVs found in C666-1 were likely due to common segmental duplications, while others could be more specific to C666-1.

In addition to indels, OMSV also identified 68 copy number variations (CNVs), 28 medium-size inversions, 13 large inversions, and 6 translocations (2 intra-chromosomal and 4 inter-chromosomal) (Additional files 3,5). A translocation in C666-1 between intron 1 of UBR5 and intron 6 of ZNF423 was previously reported, leading to a fusion transcript [36]. We were able to confirm the existence of this translocation on the list of complex SVs identified by OMSV (Figure 5).

Whole-genome sequencing data of C666-1 were previously produced at 75x coverage with 100bp paired-end reads and an average insert size of 290bp [32]. We used two sequencing-based SV callers, Manta [37] and Pindel [38], to identify large (>2kbp) SVs from the sequencing data. Among the 810 indels identified by OMSV, 552 of them (68%) were missed by both short-read based SV callers (Figure 6a). In particular, among the 543 insertions, 459 of them (85%) were missed by both. Even for the insertions detected by Manta or Pindel, they could only provide the locations of the break points but not the sizes of the insertions, which are reported by OMSV.

On the other hand, there were also some large SVs called by the short-read based methods but not by OMSV. On the basis of the assumption that SVs identified by at least two methods are more likely to be real, we found that OMSV had the highest fraction of deletions belonging to this category of high-confidence SVs ( $174/267=0.65$ ) as compared to Manta ( $264/6534=0.04$ ) and Pindel ( $215/742=0.29$ ). Since Pindel did not call any large insertions, we could not perform this analysis on the insertions.

We further investigated the 111 non-redundant deletions commonly called by Manta and Pindel but not by OMSV. We found that 2 overlapped with N-gaps in the reference genome or fragile sites and 34 were in regions with low optical map coverage, both representing SVs impossible to be detected by OMSV based on the data produced. Another 18 cases were missed by OMSV due to errors in the alignment of optical maps. There were 33 cases in which the alignments of optical maps were good but did not support an SV, which could mean either the optical maps supporting the SVs were not aligned successfully, or the SVs identified by the short-read based callers were false positives. Amount the remaining cases, 19 had low likelihood scores that could not pass the OMSV parameter threshold we chose, and 5 were missed by OMSV with no obvious reasons. The 24 SVs in these last two categories are the ones that might be detectable by improving the SV calling modules in OMSV.

Among the 115 complex SVs identified by OMSV, Manta and Pindel together could only detect 1 large inversion and 2 translocations. On the other hand, these two short-read based methods only identified 8 inversions in common, with none of the 116 translocations detected by Manta also detected by Pindel.

To further check the accuracy of the SVs identified by OMSV, we performed PCR validations. We focused on insertions and complex SVs, which are the types more difficult for short-read based callers to identify accurately. Considering the maximum possible product size of PCR, we selected 17 SVs for validation experiments, including 7 homozygous insertions, 7 heterozygous insertions and 3 complex SVs (Additional file 1: Tables S10-S12). For each one of them, we designed primers based on its predicted break points on the reference sequence, and compared the length of the resulting PCR-amplified product with its expected length with or without the SV (Additional file 1: Tables S10-S13, Methods).

For the homozygous insertions (Figure 6b), all 7 cases showed a single band much closer to the expected size with the insertion than the expected size without the insertion, although in one case ( $I_{o7}$ ) the band was weak.

For the heterozygous insertions (Figure 6c), the two bands having the expected product sizes with or without the insertions were seen in 4 of the 7 cases ( $I_{e2}$ - $I_{e4}$ , $I_{e7}$ ), although the one corresponding to the insertion allele was weaker in general, likely due to their longer products. Additional bands were also observed in several cases, suggesting that the insertions could be due to tandem duplications and the additional bands correspond to another copy number. For 2 of the cases ( $I_{e5}$ , $I_{e6}$ ), a band was observed at the expected size of the reference allele, while another relatively strong band was observed with a size slightly different from the expected size with the insertion, illustrating a limitation of estimating SV sizes precisely from optical maps. Finally, for 1 case ( $I_{e1}$ ), only one band was observed at the expected size of the reference allele, indicating that it could be a false positive call.

For the complex SVs (Figure 6d), in all 3 cases PCR products were seen with a size in agreement with the estimated size of OMSV.

Altogether, among the 17 validated cases, 14 were clearly validated, 2 had issues with the estimated SV size, and 1 could not be validated.

Since optical maps only estimate SV break points up to the closest nicking sites, we used the sequencing reads to determine the break points more precisely and deduce the inserted sequences in insertions by local sequence assembly (Additional file 1: Figure S9, Methods). The inferred sequences for the seven PCR-validated homozygous insertions and the precise SV

break points are all supported by a large number of aligned sequencing reads (Figure 6e, Additional file 1: Figure S10).

## Discussion

Currently, it is difficult to detect large or complex SVs from sequencing alone, and even harder to estimate SV sizes, due to short read length and limited insert size between read pairs. In particular, large insertions are especially difficult to be detected by short-read based SV calling methods since alignment of supporting reads that contain contents not in the reference is difficult, and read coverage is only locally dropped around the insertion site. Having repeat elements around the SV break points could also make SV detection from short sequencing reads difficult. In contrast, using nanochannel-based optical maps, whole SVs are easily contained in a single optical map, making SV detection highly feasible and accurate. Here we demonstrated that OMSV is a powerful tool for identifying large SVs from kilobases to more than a hundred kilobases. In fact, as long as an optical map can be correctly aligned to the reference by having sufficient nicking sites in the flanking non-SV portions, the larger an SV is, the easier for it to be detected by OMSV, since the corresponding distance change between the defining nicking sites is less likely due to scaling and measurement errors alone. This property makes OMSV an ideal complement to sequencing-based SV callers, which are generally more accurate in detecting smaller SVs.

For complex regions and very large SVs, OMSV detects them by employing a two-round alignment strategy that allows split-alignment of an optical map to multiple locations on the genome. Split-alignments of optical maps could come with a cost of extra alignment time. One way to tackle this problem is to first quickly align optical maps that can be aligned to single genomic loci using a standard aligner, and then apply the split-alignment strategy only to the remaining unaligned optical maps.

Since the SV calling modules only require a list of optical map alignments as input, the alignment methods used in the OMSV pipeline can be flexibly changed to other choices. Besides, if a high-quality *de novo* assembly of the optical maps is available, the optical maps can also be first aligned to the assembly, and their alignment to the reference can then be inferred from the further aligning the assembly to the reference. For optical maps that deviate significantly from the reference map, this two-step alignment strategy could be more accurate than directly aligning optical maps to the reference.

With each optical map coming from one DNA molecule, OMSV can potentially be extended to study

haplotypes, cell type composition in a sample and cell-to-cell variability. These analyses would require highly accurate alignments of individual labels of the optical maps. Probing the nicking sites of a second enzyme using an additional color channel may further improve alignment accuracy necessary for these analyses. With such improved accuracy, we also hope to extend OMSV to call the zygosity of complex SVs.

## Conclusions

In this paper, we described the OMSV pipeline for identifying SVs from nanochannel-based optical maps. The accuracy of OMSV has been confirmed by both simulations and optical maps from a family trio. OMSV outperformed the only publicly available tool for SV detection from OM data in three aspects, namely 1) OMSV identified many more SVs at a precision level similar to this method, 2) OMSV identified many of the complex SVs but this method missed all of them, and 3) OMSV ran much faster by not requiring a time-consuming *de novo* assembly of the optical maps.

We also used OMSV to identify SVs from the C666-1 cell line, and found 68% of them missed by sequencing-based SV callers, including 85% of the insertions. Some of these SVs were experimentally validated independently.

We provide OMSV as open-source software, which can be used routinely in genome projects to accurately and comprehensively identify large SVs that will likely have important implications for understanding genetic diversity and disease susceptibility.

## Methods

### A complete error model for optical maps

We modeled the generation of optical maps from a DNA sequence as a random process with various types of error, which combines some ideas previously proposed [19, 21] and several new components based on properties observed in real human optical maps [28].

In our model, the starting locations of  $n$  DNA fragment molecules are first uniformly and independently sampled from the DNA sequence. Each of these starting locations is used to produce a molecule with length  $l_0 + l_v$ , where  $l_0$  is a constant minimum molecule length, and  $l_v$  is a random variable that follows a Poisson distribution with mean  $\mu_l$ . In real experiments,  $l_0$  is a threshold chosen such that molecules shorter than it are excluded from the analyses.

The restriction sites on each molecule can be identified by matching its sequence against the recognition motif of the nicking enzyme selected. In our model, each restriction site has a false negative rate of  $f_-$  for

not having a corresponding observable label in the optical map due to incomplete enzymatic digestion or a measurement error.

False positive labels not originated from actual restriction sites but caused by artifacts such as non-specific enzymatic cuts are then introduced. For every two adjacent restriction sites, the number of false positive labels is randomly sampled from a Poisson distribution with mean  $df_+$ , where  $d$  is the distance between the two sites and  $f_+$  is the false positive rate. If the resulting number of false positive labels is non-zero, the occurrence locations of these false positives are uniformly and independently sampled from the locations between the two sites.

After these steps, each random molecule is represented by a list of distances between adjacent observed labels (including both true positives and false positives). For the convenience of discussion, we also assume the beginning and end of each molecule are marked by two artificial labels, the locations of which in actual optical maps can be determined by the span of the stained DNA backbone. Each molecule then undergoes a random stretch / compression to model sizing errors in the experiments, by multiplying the distance between every two observed labels by a factor  $\alpha$ , where  $\alpha$  is sampled from a Cauchy distribution with the values of the location and scale parameters set to  $o_\alpha$  and  $s_\alpha$ , respectively. We chose the Cauchy distribution since it had a good fit with the real data we produced (Additional file 1: Figure S11).

To model the finite resolution of optical measurements, for any two adjacent labels on a stretched / compressed molecule at a distance of  $d$  bp from each other, they are merged into one single label that occurs at the mid-point of them with a probability of  $1 - \frac{1}{1 + \exp\left[-\frac{1}{0.01(d-d_{\frac{1}{2}})}\right]}$ , where  $d_{\frac{1}{2}}$  is a reference distance at which the chance for two labels to be merged is 1/2.

Finally, measurement errors are modeled by moving each label by an offset that follows a uniform distribution defined on  $[-e, e]$  for a given parameter  $e$ .

### SV calling modules

Based on the above generative model, we developed two statistical modules for identifying SVs from optical maps. The first module looks for individual extra or missing sites on the molecules as compared to the reference sequence. Some small SVs with only a mild change of the distance between restriction sites are better detected by this method. The second module compares the distance between two restriction sites on the molecules with that on the reference genome, which can detect larger SVs not necessarily involving extra/missing restriction sites.

Both modules require an alignment of the optical maps to a reference map obtained from the *in silico* digestion of the reference sequence, where the adjacent labels are also merged by the way described in the above section. Based on the alignments, OMSV extracts three types of information as inputs to the two SV calling modules, namely 1) the expected locations of restriction sites on the reference sequence, 2) the distance (in bp) between every two adjacent observed labels on each molecule, and 3) an alignment of the labels on the molecules to the restriction sites on the reference. Every label can be aligned to zero or one restriction site on the reference, and each restriction site on the reference can be aligned to zero or one label on each molecule.

The third module uses some additional alignment and coverage information to identify complex SVs.

### Module for identifying SVs involving extra or missing restriction sites

To identify missing restriction sites on the molecules, we adopted a method originally developed for refining optical map assemblies [20], and extended it to detect both homozygous and heterozygous genetic variants.

Suppose there are  $M$  molecules aligned to a region that covers a restriction site on the reference sequence, among which  $m$  supports the existence of the restriction site (Figure 2a). Each of the  $m$  supporting molecules either actually contains the site or has a false positive label. Each of the  $M - m$  non-supporting molecules either actually does not contain the site or has a false negative. We consider three hypotheses for the observed data, namely 1) the null hypothesis  $H_0^{(miss)}$  that the restriction site actually exists on the subject DNA sequence in homozygous form (and thus there are no false positives), 2) the first alternative hypothesis  $H_{hom}^{(miss)}$  that the site is missing on the subject sequence in homozygous form (and thus there are no false negatives), and 3) the second alternative hypothesis that the site is missing on the subject sequence in heterozygous form.

Under the null hypothesis  $H_0^{(miss)}$ , the probability of observing  $m$  or fewer supporting molecules is

$$\Pr(x \leq m | H_0^{(miss)}) = \sum_{x=0}^m \binom{M}{x} (1 - fn)^x fn^{M-x},$$

where  $fn$  is the false negative rate to be estimated from the observed data. Similarly, depending on whether  $H_0^{(miss)}$ ,  $H_{hom}^{(miss)}$  or  $H_{het}^{(miss)}$  is true, the data likelihood is respectively

$$L_{H_0^{(miss)}} = \binom{M}{m} (1 - fn)^m fn^{M-m},$$

$$L_{H_{hom}^{(miss)}} = \binom{M}{m} fp^m (1 - fp)^{M-m}, \text{ and}$$

$$L_{H_{het}^{(miss)}} = \sum_{k=0}^M \left\{ \binom{M}{k} \left(\frac{1}{2}\right)^M \sum_{l=\max(0, m-M+k)}^{\min(k, m)} \binom{k}{l} (1 - fp)^l fp^{k-l} \binom{M-k}{m-l} fp^{m-l} (1 - fp)^{M-k-m+l} \right\} k$$

where  $fp$  is the false positive rate to be estimated from the observed data,  $k$  is, in the heterozygous case, the unknown number of molecules coming from the chromosome with the restriction site, and  $l$  is the number of molecules among the  $k$  on which the restriction site is observed. In the model, we assume there is an equal probability for a molecule to come from either chromosome.

Based on these definitions, if both the p-value  $Pr(x \leq m | H_0^{(miss)})$  and the likelihood ratio  $L_{H_0^{(miss)}} / \max(L_{H_{hom}^{(miss)}}, L_{H_{het}^{(miss)}})$  are smaller than corresponding thresholds for a site, it is considered a homozygous missing site if  $L_{H_{hom}^{(miss)}} \geq L_{H_{het}^{(miss)}}$  and a heterozygous missing site if  $L_{H_{hom}^{(miss)}} < L_{H_{het}^{(miss)}}$ .

A similar procedure is used for calling homozygous and heterozygous extra restriction sites. Suppose there are  $M$  molecules aligned to a region on the reference sequence, among which  $m$  supports the existence of a restriction site in the region that does not exist according to the reference sequence. Under the null hypothesis  $H_0^{(extra)}$  that the site is absent in homozygous form, the probability of observing  $m$  or more supporting molecules is

$$Pr(x \geq m | H_0^{(extra)}) = \sum_{x=m}^M \binom{M}{x} fp^x (1 - fp)^{M-x}.$$

Similarly, depending on whether the site is absent in homozygous form (null hypothesis  $H_0^{(extra)}$ ), exists in homozygous form (alternative hypothesis  $H_{hom}^{(extra)}$ ), or exists in heterozygous form (alternative hypothesis  $H_{het}^{(extra)}$ ), the data likelihood is respectively defined as

$$L_{H_0^{(extra)}} = L_{H_{hom}^{(miss)}},$$

$$L_{H_{hom}^{(extra)}} = L_{H_0^{(miss)}}, \text{ and}$$

$$L_{H_{het}^{(extra)}} = L_{H_{het}^{(miss)}}.$$

Based on these definitions, if both the p-value  $Pr(x \geq m | H_0^{(extra)})$  and the likelihood ratio  $L_{H_0^{(extra)}} / \max(L_{H_{hom}^{(extra)}}, L_{H_{het}^{(extra)}})$  are smaller than corresponding thresholds for a site, it is considered a homozygous extra site if  $L_{H_{hom}^{(extra)}} \geq L_{H_{het}^{(extra)}}$  and a heterozygous extra site if  $L_{H_{hom}^{(extra)}} < L_{H_{het}^{(extra)}}$ .

In practice, we also define a minimum number of supporting molecules  $M_{min}$ . For any site with less than  $M_{min}$  molecules covering the locus (no matter supporting the presence of the restriction site or not), we did not call genetic variants from it since the result would not be reliable.

#### Module for identifying SVs involving large size changes

Large SVs are usually associated with a deviation of the distance between two restriction sites on the reference sequence (Figure 2b,  $d_0$ ) and that on the molecules ( $d_1$ ), which may or may not involve extra/missing restriction sites on the molecules. To systematically identify these cases, we first check the distances between every two adjacent restriction sites on the reference sequence and compare them with the corresponding label distances on the aligned molecules (which would cover the first two cases of Figure 2b). We then check the distances between every two adjacent labels on the aligned molecules that have not been checked, and compare them with the distance between the aligned restriction sites on the reference (which would cover the third case). Each of these checks is performed by the following statistical method.

Suppose there are two (not necessarily adjacent) restriction sites on the reference sequence with a distance  $d_0$ , and there are  $M$  aligned molecules covering the region. Suppose the distances of the corresponding aligned labels on the molecules are  $d_1, d_2, \dots, d_M$ , where  $d_1 \leq d_2 \leq \dots \leq d_M$ . Our method computes the ratios  $r_i = \frac{d_i}{d_0}$  for each of the  $M$  molecules. It then compares the following hypotheses according to the error model we defined:

- 1 Null hypothesis  $H_0$ , that there are no insertions or deletions between the two sites
- 2  $H_{hom}$ , that there is a homozygous indel between the two sites
- 3  $H_{het}^{(ins)}$ , that there is a heterozygous insertion between the two sites
- 4  $H_{het}^{(del)}$ , that there is a heterozygous deletion between the two sites
- 5  $H_{tri}$ , that the locus is triallelic, i.e., there are two different insertions, two different deletions, or one insertion and one deletion between the two sites, where each chromosome bears one of the two variant alleles

Under the null hypothesis  $H_0$ , the likelihood of observing the distance ratios  $r_1, r_2, \dots, r_M$  is

$$L_{H_0} = \prod_{i=1}^M Cauchy(r_i, r_0, \gamma),$$

where  $Cauchy(r_i, r_0, \gamma) = \frac{\gamma}{\pi[(r_i - r_0)^2 + \gamma^2]}$  is the probability density function of the Cauchy distribution with

position parameter  $r_0$  and scale parameter  $\gamma$ . In SV detection, using the Cauchy distribution to model the distance ratios has an advantage that it is not heavily affected by extreme outliers caused by alignment errors.

Under the alternative hypothesis  $H_{hom}$ , the distance ratios  $r_1, r_2, \dots, r_M$  are sampled from a Cauchy distribution with a different value for the location parameter but the same value  $\gamma$  for the scale parameter. The likelihood of observing the distance ratios is therefore

$$L_{H_{hom}} = \prod_{i=1}^M \text{Cauchy}(r_i, r'_0, \gamma),$$

where  $r'_0$  is the location parameter of the distribution of distance ratios for this indel event. Finding the maximum likelihood estimate of  $r'_0$  would require the use of numerical methods to solve a high-degree polynomial. Instead, we used the sample median of the  $M$   $r_i$ 's as an imperfect estimate [39].

Under the alternative hypothesis  $H_{het}^{(ins)}$ , some of the distance ratios are sampled from the null distribution and the others are sampled from an alternative Cauchy distribution with a larger value  $r'_0$  for the location parameter but the same value for the scale parameter. The likelihood of the distance ratios is  $L_{H_{het}^{(ins)}} = \frac{1}{2^M} \sum_{S \subset \{1, 2, \dots, M\}} \left[ \prod_{j \notin S} \text{Cauchy}(r_j, r_0, \gamma) \prod_{i \in S} \text{Cauchy}(r_i, r'_0, \gamma) \right]$ , where  $S$  represents the set of molecules from the chromosome with the insertion, assuming an equal probability for each molecule to come from either chromosome. Practically, this likelihood is difficult to compute due to the exponential number of terms in the summation. We made an assumption that the two distributions are sufficiently separated, with  $|r'_0 - r_0| \gg \gamma$ . Based on this assumption, we consider only the summation terms of which  $S$  takes the form  $\{r_{M-k+1}, r_{M-k+2}, \dots, r_M\}$ , which involves only the  $k$  largest distance ratios. We then try all possible values of  $k$  such that at least  $k_{min}$  molecules come from each chromosome (Figure 2c). As a result, the likelihood formula is simplified as  $L_{H_{het}^{(ins)}} = \frac{1}{2^M} \sum_{k=k_{min}}^{M-k_{min}} \left[ \prod_{i=1}^{M-k} \text{Cauchy}(r_i, r_0, \gamma) \prod_{j=M-k+1}^M \text{Cauchy}(r_j, \tilde{\mu}_{M-k+1..M}, \gamma) \right]$ , where  $\tilde{\mu}_{M-k+1..M}$  is the sample median of  $r_{M-k+1}, r_{M-k+2}, \dots, r_M$ .

Similarly, for heterozygous deletions, a simplified likelihood formula is defined as

$L_{H_{het}^{(del)}} = \frac{1}{2^M} \sum_{k=k_{min}}^{M-k_{min}} \left[ \prod_{i=1}^k \text{Cauchy}(r_i, \tilde{\mu}_{1..k}, \gamma) \prod_{j=k+1}^M \text{Cauchy}(r_j, r_0, \gamma) \right]$ , where  $\tilde{\mu}_{1..k}$  is the sample median of  $r_1, r_2, \dots, r_k$ , is expected to be smaller than  $r_0$  in this case (and a heterozygous deletion would not be called if this expectation is not satisfied).

For the triallelic cases, the simplified likelihood formula is defined as

$L_{H_{tri}} = \frac{1}{2^M} \sum_{k=k_{min}}^{M-k_{min}} \left[ \prod_{i=1}^k \text{Cauchy}(r_i, \tilde{\mu}_{1..k}, \gamma) \prod_{j=k+1}^M \text{Cauchy}(r_j, \tilde{\mu}_{k+1..M}, \gamma) \right]$ , where  $\tilde{\mu}_{1..k}$  is the median of  $r_1, r_2, \dots, r_k$  and  $\tilde{\mu}_{k+1..M}$  is the median of  $r_{k+1}, r_{k+2}, \dots, r_M$ .

Finally, our method compares the likelihood values.

If the likelihood ratio  $\frac{L_{H_0}}{\max\{L_{H_{hom}}, L_{H_{het}^{(ins)}}, L_{H_{het}^{(del)}}, L_{H_{tri}}\}}$

is smaller than a threshold, an SV is called according to the following rules: If  $\max\{L_{H_{hom}}, L_{H_{het}^{(ins)}}, L_{H_{het}^{(del)}}, L_{H_{tri}}\}$  is equal to

- $L_{H_{hom}}$ : If  $r'_0 > r_0$ , a homozygous insertion is called; Otherwise, a homozygous deletion is called.
- $L_{H_{het}^{(ins)}}$ : A heterozygous insertion is called.
- $L_{H_{het}^{(del)}}$ : A heterozygous deletion is called.
- $L_{H_{tri}}$ : An SV of the ‘‘multiple’’ type is called. If  $\tilde{\mu}_{1..k}$  and  $\tilde{\mu}_{k+1..M}$  are both smaller than  $r_0$ , two different deletions are called; If both are larger than  $r_0$ , two different insertions are called; Otherwise, an insertion and a deletion are called.

Practically, if the distance change is too small, either absolutely or relative to the distance on the reference, the SV calls are less reliable. We therefore keep only SVs with a distance change larger than a threshold  $\delta$ , where the distance on the molecules is defined as the median distance of the set of molecules that lead to a term with the largest value in the likelihood calculation.

#### Module for identifying complex SVs

We also developed a module for identifying three types of complex SVs, namely inversions, translocations and CNVs.

*Using split-alignment to identify large inversions and translocations:* The split-alignment capability of OMBlast [22] allows different parts of a single optical map to be separately aligned to different locations of the same chromosome (Figure 2d). The default setting of OMBlast limits the maximum distance between these different locations to reduce false alignment rate, and thus it permits direct calling of only intra-chromosomal translocations involving close loci. To detect other intra-chromosomal translocations and inter-chromosomal translocations, we used a 2-round alignment strategy (Figure 2e), in which the first round performed standard alignments of optical maps, with some optical maps only partially aligned. For these optical maps, the unaligned regions were then independently aligned again in the second round, thus allowing the detection of all types of translocations. In addition, by allowing different portions of the same optical map to be aligned in different orientations, large inversions can also be detected. To reduce false positives, only translocations and large inversions supported by two or more optical maps are considered.

*Using reverse-palindromic CIGAR strings to identify medium-sized inversions:* Inversions with size between 2kbp and 100kbp can be contained in a single optical map, and are detected by locating a region in an optical map alignment with 1) a reverse-palindromic CIGAR (Compact Idiosyncratic Gapped Alignment Report) string; and 2) matching distances between adjacent restriction sites on the reference and those between adjacent labels on the reversed optical map (Figure 2f). In a CIGAR string, a matched, missing and extra label is denoted as ‘M’, ‘D’ and ‘I’, respectively. The reverse-complement of a CIGAR string is the reverse of it with ‘I’s and ‘D’s interchanged. For example, the reverse-complement of MDDI is DIIM. A CIGAR string is reverse-palindromic if it is the same as its reverse-complement, such as DIDIDI. Two distances  $d_1$  and  $d'_1$  are considered matched if  $d_1 \times (1 - e_t) - e_m \leq d'_1 \leq d_1 \times (1 + e_t) + e_m$ , where  $e_t$  and  $e_m$  are the maximum scaling and measurement errors (set to 0.1 and 500bp), respectively. To control the quality, we called an inversion only if it had at least 10 supporting molecules and at least 4 nicking sites within the inverted region.

*Using depth of coverage to identify CNVs:* We modified an event-wise significance testing method [40] to identify large CNVs. The original method uses a sliding window (with 100bp) to scan the reference and look for windows with a depth of coverage significantly different from other windows, based on the distribution of depths of windows with similar GC contents. Neighboring windows are then grouped into blocks to identify the span of the CNVs, with a method for correcting for multiple hypothesis testing. To adopt this method for OM data, first the window size was enlarged to  $2d_{1/2}$  to accommodate for the lower resolution of OM data, where  $d_{1/2}$  is the imaging resolution. Then to determine the statistical significance of each window, instead of grouping windows by GC content, we grouped them by nicking site counts. The depths (number of aligned optical maps) of all windows within a group were fit to a Gaussian distribution, and a window was considered a CNV candidate if it received a Z-test p-value  $< 0.05$ . The same procedure for determining CNV spans in the original method was then applied.

#### The overall OMSV pipeline

The overall OMSV pipeline is illustrated in Figure 1b. In the alignment pipeline, we used default parameter values of RefAligner and OMBlast for all the simulated and real data except C666-1, in which case we used RefAligner parameter values for complex genomes (available on our supplementary Web site) suggested by BioNano technical team. The reference map was deduced

from the human reference hg38 in all cases. RefAligner and OMBlast alignments were integrated based on the following rules:

- 1 If the two methods align an optical map to genomic regions within half the length of the optical map from each other, they are considered to agree on the alignment, and the alignment of RefAligner is taken.
- 2 If only one of the two methods can align an optical map, the alignment is taken directly.
- 3 If both methods cannot align an optical map, or both of them can align but their alignments do not agree with each other, the optical map is left unaligned.

We call this the “union” strategy in Additional file 1: Figure S6. We also considered an “intersection” strategy, which only involved the alignments satisfying the first rule above.

The resulting integrated list of alignments is sent to the three modules for SV identification. The results from the three modules are then integrated to form a final list of SVs.

The parameter values of OMSV used in our experiments are listed in Additional file 1: Table S14.

#### Filtering of SVs detected from real data

We considered only optical map alignments with a confidence score of 9 or more. For the indels identified from the family trio and the C666-1 cell line, we filtered those that overlapped N-gaps, fragile sites or pseudo-autosomal regions on the reference genome. These “mask” regions are listed in Additional files 6–8. We applied the same filtering to the NA12878 SV lists obtained from sequencing-based methods. For the complex SVs, we filtered the ones located within the pseudo-autosomal regions or overlapped with the regions with ultra-high density of nicking sites, defined as regions spanning 200kbp or more with at least 333 nicking sites per 1Mbp. This density threshold was chosen because it corresponds to having an average distance between adjacent nicking sites of 3kbp, which makes it hard to detect complex SVs accurately.

#### Generation of simulated data

We generated simulated data with either only homozygous variants or both homozygous and heterozygous variants. Two steps were involved in both cases, namely a first step for generating genomic sequences with genetic variations introduced to the human reference genome, and a second step for simulating optical maps based on the resulting genomic sequences using the error model described above.

### *Simulated data with only homozygous variants*

For the data set with homozygous variants only, we first downloaded the human reference sequence hg38 from the UCSC Genome Browser [41]. We then generated mutations (single nucleotide variants, small and large indels, and complex SVs) on it using pIRS (profile based Illumina pair-end Reads Simulator) [42]. This software was originally developed for generating short sequencing reads. We took its intermediate file containing the mutated sequence without generating the short reads. In the second step, we used the mutated sequence as input to generate simulated optical maps based on our generative model. The parameter values used in the two steps are shown in Additional file 1: Table S15 and Additional file 1: Table S16, respectively. The parameter values for the first step were determined based on corresponding estimates from human genomes reported in previous studies [43–45]. The parameter values for the second step were estimated from our actual optical maps by aligning all molecules to the reference sequence using RefAligner, and estimating the parameter values by likelihood maximization. All these parameter values were not made known to our SV detection methods.

### *Simulated data with both homozygous and heterozygous variants*

For the data set with both homozygous and heterozygous variants, we generated a diploid genome as follows. It was initialized by our generated haploid genome and the reference genome as the two haplotypes. Then for each variant on the first haploid genome, it received a probability of  $p_{hom}$  to be copied to the second haploid genome, resulting in a homozygous variant. For the remaining variants, which would remain heterozygous, each of them received a probability of  $p_{het}$  of moving from the first haploid genome to the second. We used  $p_{hom} = 0.5$  and  $p_{het} = 0.5$  in our simulations based on a previous study [46]. As a result of this procedure, the total number of SV loci in this diploid genome was the same as that in the haploid genome.

We then considered the two haploid genomes together as a diploid genome, and used the corresponding DNA sequences as the templates to produce OM data using our generative model. The parameter values used in the two steps of simulation are again shown in Additional file 1: Table S15 and Additional file 1: Table S16, and 26 additional data sets were generated by changing the false positive rate, false negative rate and depth of coverage, as shown in Additional file 1: Table S2.

### **Evaluation metrics of SV calling on simulated data**

For the simulated data, we used the known locations of the generated SVs to compute the precision (fraction of identified SVs that are real) and recall (fraction of real SVs that are identified) rates of an SV calling method. An SV call was considered correct if it overlapped the location of a generated SV of the same type.

### **Comparison with BioNano Solve**

We compared OMSV with the SV caller included in BioNano Solve v3.0 (downloaded from <https://bionanogenomics.com/support/software-downloads/>), which was the only SV caller for nanochannel-based optical maps with publicly available software. The exact command-line arguments used can be found on the supplementary Web site.

### **Evaluating the performance of OMSV in the ideal situation with no alignment errors**

To estimate the performance of OMSV in the ideal situation with no alignment errors, instead of supplying optical map alignments as inputs to OMSV, we provided observed-to-reference distance ratios between neighboring nicking sites directly. For each locus, the number of distance ratios was drawn from a Gaussian distribution estimated based on the depth of coverage of the data set. The values of these distance ratios were produced by adding scaling errors to the actual distance ratio of the corresponding allele based on the sizing error parameter of the default simulated data set. The ratio of loci with and without SVs also followed the ratio in the default data set.

### **Evaluation metrics of alignment pipeline on simulated data**

We also defined metrics for evaluating the performance of our alignment pipeline. First, an optical map was considered correctly aligned if it was aligned to the correct haplotype of the simulated genome with the aligned location overlapping the actual location from which the optical map was generated. Alignment precision was then defined as the fraction of aligned optical maps that were correctly aligned, and recall was defined as the fraction of generated optical maps that were correctly aligned.

### **Integrating and de-duplicating indels from the trio**

In the comparisons with manual checking results and the SVs reported in the two previous studies [2, 30], we first integrated the indels from the three individuals. For indels that overlapped, we de-duplicated them by merging them into a larger indel that spanned over all these original indels. For each resulting indel, we considered it contained by an individual if the individual originally had an indel that overlapped it.

### Definition of Mendelian concordance

For the family trio, a locus was defined as concordant with Mendelian inheritance if the daughter's genotype could be produced by the genotypes of the father and the mother. When zygosity was not considered, an SV identified from an individual could mean that the individual had the SV in homozygous or heterozygous form. As a result, a Mendelian error was reported only when the daughter had an SV at a locus of a type that both parents did not have. When zygosity was considered, a Mendelian error was reported when the two alleles of the daughter could not respectively come from the two parents. For this part of analysis, we considered only loci at which each of the individuals either had an SV confidently called, or it was highly unlikely that an SV could be called. The former was defined as SVs with at least 10 supporting optical maps and a likelihood ratio of at most  $10^{-6}$  for each other hypothesis. The latter was defined as cases in which an SV could not be called even at the loose thresholds of 4 supporting optical maps and a likelihood ratio of 1.

### Computation of expected Mendelian concordance

In order to check whether the observed Mendelian concordance values of the SVs identified from the trio were consistent with the precision and recall estimates of our simulation, we computed the expected Mendelian concordance values as follows. First, we estimated the probabilities  $P(G_2|G_1)$  where  $G_1$  and  $G_2$  are respectively the actual genotype and the genotype called by OMSV, each with possible alleles  $A$  (the reference allele) and  $a$  (the alternative allele). The probabilities  $P(aa|aa)$ ,  $P(Aa|aa)$ ,  $P(AA|aa)$ ,  $P(aa|Aa)$ ,  $P(Aa|Aa)$  and  $P(AA|Aa)$  were all estimated based on the fraction of homozygous and heterozygous variants generated in our simulated data that were called by OMSV to have the corresponding genotypes. For the remaining three conditional probabilities,  $P(Aa|AA) = P(AA|Aa)P(Aa)/P(AA) \approx P(AA|Aa)P(Aa)$ , where  $P(AA|Aa)$  was again estimated from our simulation result, and  $P(Aa)$  was estimated as half the prior SV probability of the human genome,  $8 \times 10^{-3}/2$  (based on the median total SV size of 20Mbp per individual reported in Sudmant et al. [2]), assuming equal probability for homozygous and heterozygous SVs.  $P(aa|AA)$  was estimated in exactly the same way. Finally,  $P(AA|AA) = 1 - P(Aa|AA) - P(aa|AA)$ .

With all these 9 probabilities computed, we charted the probability for each combination of actual and called genotypes of the trio. Specifically, the father, mother and daughter genotypes were denoted as a triple. For example,  $(AA, aa, Aa)$  represents the situation that the father has the reference genotype, the mother has an SV in homozygous form

and the daughter has the SV in heterozygous form. The probability for an actual genotype combination  $C_1$  to be called as a genotype combination  $C_2$  was calculated as the product of the three corresponding conditional probabilities, assuming SV calling errors of the three individuals are independent. For example,  $P((AA, AA, aa)|(AA, aa, Aa)) = P(AA|AA)P(AA|aa)P(aa|Aa)$ .

When zygosity was considered, the actual genotype combination must come from the set of 15 combinations concordant with Mendelian inheritance,  $O = \{(AA, AA, AA), (AA, aa, aa)\}$ . The overall expected Mendelian concordance rate was then calculated as  $\sum_{C_1 \in O} [P(C_1) \sum_{C_2 \in O} P(C_2|C_1)]$ . We estimated the prior probabilities  $P(C_1)$  by the number of times such genotype combination was called by OMSV in the trio data.

When zygosity was ignored, the expected Mendelian concordance rate was calculated as  $1 - \sum_{C_1 \in S} P(C_1) [P(AA, AA, Aa|C_1) + P(AA, AA, aa|C_1)]$ .

### Comparing with sequencing-based results for NA12878 SVs

We lifted over the SV lists of NA12878 from Parikh et al. [30] and Sudmant et al. [2] from hg19 to hg38. We then filtered both these lists and our list of SVs by removing SVs with a size smaller than 2,000bp or overlapping the mask regions. The remaining SVs on the three lists were then compared.

### Production of optical maps from C666-1

#### *High-molecular-weight DNA extraction*

The C666-1 cell line was washed with PBS and spun down to pellet.  $10^6$  cell/mL were obtained upon resuspension in PBS, and embedded in 1.5% low-melting agarose plugs in 0.5x TBE (CHEF Genomic DNA Plug Kit, Bio-Rad). Subsequent handling of the DNA followed BioNano Genomics recommended protocols: the agarose plugs were incubated with proteinase K with Lysis Buffer at 50°C overnight. The plugs were washed by Wash Buffer to stabilize DNA in plugs, and the quality was assessed using pulsed-field gel electrophoresis. A plug was then washed with TE buffer and melted in 70°C. After being solubilized with 0.4 U of GELase (Epicentre), the purified DNA was subjected to 2.5hr of drop-dialysis and was shredded by 9 strokes of gentle pipetting. The viscous DNA was allowed to equilibrate overnight at room temperature to increase homogeneity. It was then quantified using a Qubit Broad Range dsDNA Assay Kit (Life Technologies).

### DNA labeling

The DNA was labeled using the IrysPrep Reagent Kit (BioNano Genomics). Specifically, 300 ng of purified genomic DNA was nicked with 0.3U of nicking endonuclease Nt.BspQI (New England BioLabs) at 37° for 2 hr in buffers BNG3. The nicked DNA was labeled with a fluorescent-dUTP nucleotide analog using Taq polymerase (NEB) for 1 hr at 72°. After labeling, the nicks were ligated with Taq ligase (NEB) in the presence of dNTPs. The backbone of fluorescently labeled DNA was counterstained with YOYO-1 (BioNano Genomics IrysPrep Reagent Kit).

### Data collection and assembly

The DNA was loaded onto the BioNano Genomics IrysChip and linearized and visualized by the Irys system. The DNA backbone length and locations of fluorescent labels along each molecule were detected using the Irys software. Single-molecule maps were assembled *de novo* into genome maps using the IrysSolve software tools developed at BioNano Genomics [15].

### Comparing C666-1 indels with human segmental duplications

We downloaded segmental duplication regions in the human reference genome hg38 from the UCSC Genome Browser, and annotated them with gene information for those overlapping gene exons. We then compared the C666-1 indels identified by OMSV with these segmental duplication regions to look for overlaps.

### Identifying SVs from C666-1 using short reads

We used the default settings of Manta and Pindel to identify SVs from the sequencing data of C666-1. We considered only large (>2kbp) SVs supported by at least 20 reads/read pairs.

### Selection of C666-1 SVs for experimental validations

We selected SVs identified by OMSV from C666-1 cells for experimental validations based on the following two criteria, namely 1) We only selected insertions and complex SVs, since these SVs are particularly difficult to identify and their sizes difficult to determine from sequencing reads alone, and 2) We selected SVs with primers that could be designed from non-repeat regions and which would lead to amplicons analyzable by PCR. The selected SVs and the primers designed are listed in Additional file 1: Tables S10-S13.

### Integrating sequencing reads to infer precise break points and inserted sequences

For each homozygous insertion identified by OMSV from C666-1 that occurs within the region  $[o_1, o_2]$  of the human reference genome sequence hg38 with an

estimated size of  $s$ , we performed the following steps (Additional file 1: Figure S9, Additional file 1: Table S10):

- 1 Construct a tentative C666-1 sequence by replacing the region  $[o_1, o_2]$  by  $x$  copies of  $N$  (i.e., unknown) nucleotides, where  $x = o_2 - o_1 + s$  for an insertion and  $x = o_2 - o_1 - s$  for a deletion.
- 2 Use GapCloser [47] to infer the actual sequence of this  $N$  region based on local assembly of sequencing reads and the flanking sequences, which may or may not resolve all the  $N$ s.
- 3 Align sequencing reads to the region  $[o_1, o_2]$  of the reference sequence using BWA [48], visualizing only read pairs with both sides aligned using IGV [49].
- 4 Align sequencing reads to the inferred C666-1 sequence using BWA, visualizing only read pairs with both sides aligned.
- 5 Use the alignment results to evaluate confidence of the SV, the break points and the inserted sequences in the case of insertions.

### List of abbreviations

bp - base pair  
 CNV - copy number variation  
 EBV - Epstein-Barr Virus  
 IF - intrinsically feasible  
 Indel - insertion and deletion  
 kbp - kilo base pair  
 mbp - mega base pair  
 OM - optical mapping  
 PCR - polymerase chain reaction  
 SV - structural variation

### Declarations

Ethics approval and consent to participate  
 Not applicable

Consent for publication  
 Not applicable

### Availability of data and materials

All optical mapping data involved in this study are available on zenodo (<http://doi.org/10.5281/zenodo.886387>). Source code of OMSV is available on github (<https://github.com/moziya/OMSV/tree/v1.0>) and zenodo (<http://doi.org/10.5281/zenodo.1035506>). Our supplementary web site (<http://yiplab.cse.cuhk.edu.hk/omsv/>) provides the compiled package of OMSV, detailed instructions for using the package, and links to the github and zenodo entries.

The complex SV and large indel callers of OMSV were implemented in C++ and Linux bash script, and the CNV caller was implemented in Matlab R2011b (7.13.0.564) 64-bit (glnxa64). The whole package requires at least 4GB of physical memory and has been tested on both Debian GNU/Linux 9.0 (stretch) and CentOS Linux release 7.3.1611 (Core) platforms.

### Competing interests

Ernest Lam and Han Cao were employees of BioNano Genomics at the time of the study, and they owned company stock options. Han Cao and Ming Xiao were inventors of several patents owned by BioNano Genomics. The technology platform (BioNano Genomics Irys™) described in this paper was developed by BioNano Genomics.

#### Funding

T-FC and KYY are partially supported by the HKSAR Food and Health Bureau Health and Medical Research Fund HMRF12110542 and Theme-based Research Scheme T12-402/13-N. KWL, T-FC and KYY are partially supported by the HKSAR Research Grants Council Theme-based Research Scheme T12-401/13-R. AK-YL and T-FC are partially supported by the HKSAR Research Grants Council General Research Fund 14102014 and Area of Excellence Scheme (AoE/M-403/16).

#### Authors' contributions

T-FC and KYY conceived the study. LL, AK-YL, T-PK, ML, JJKW, S-MY, T-FC and KYY designed the computational methods. LL, AK-YL and T-PK implemented the computational methods. GT-YC and K-WL prepared C666-1 DNA. LL, AK-YL, YYYY, ACYM, AP, CC, ETL, HC, CL, JS, MX, P-YK and T-FC produced and processed optical mapping data. LL, AK-YL, IKP, T-FC and KYY designed validation experiments. AK-YL and IKP performed validation experiments. LL, AK-YL, T-PK, T-FC and KYY wrote the manuscript. All authors read and approved the final manuscript.

#### Author details

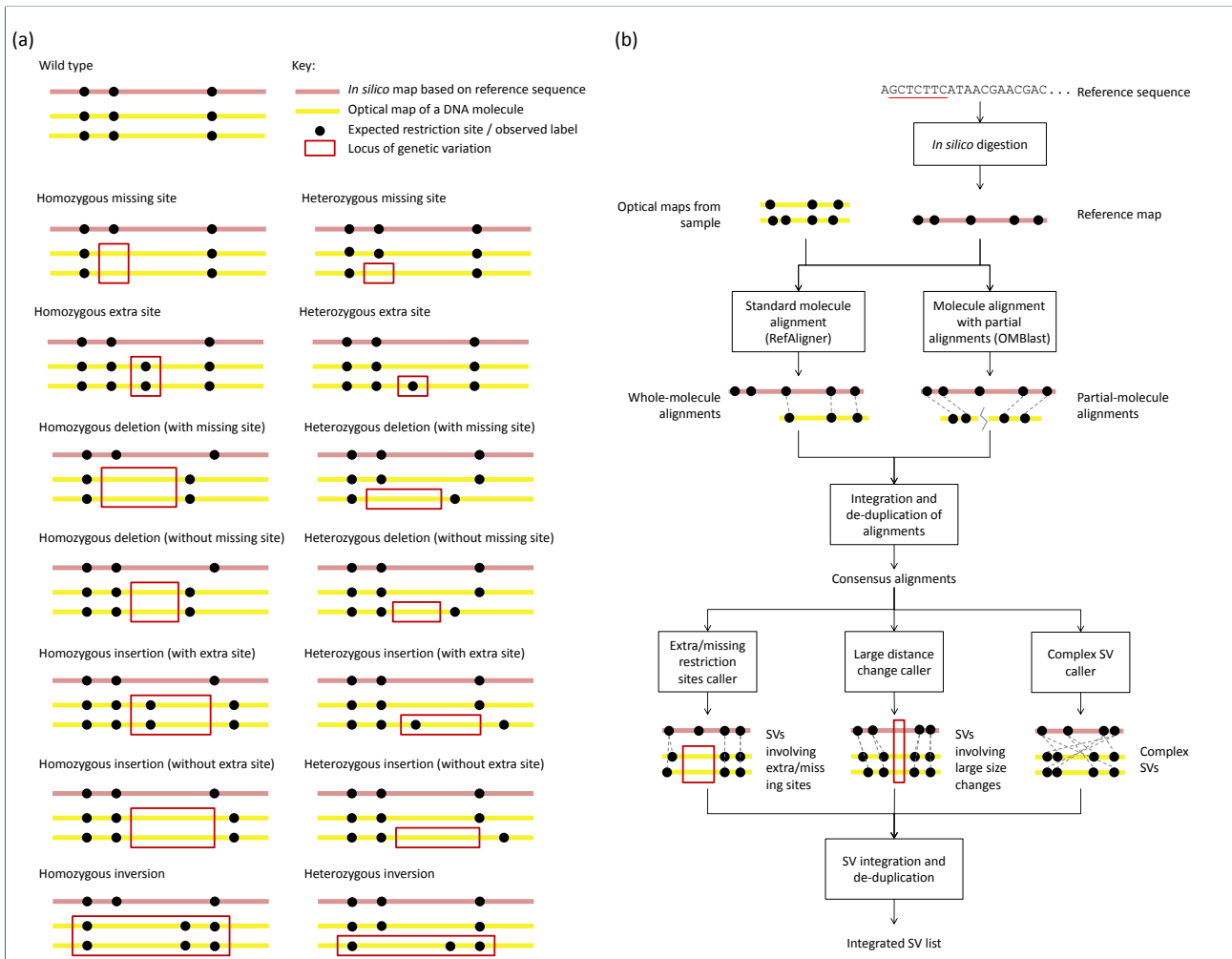
<sup>1</sup>Department of Computer Science and Engineering, The Chinese University of Hong Kong, Shatin, New Territories, Hong Kong. <sup>2</sup>School of Life Sciences, The Chinese University of Hong Kong, Shatin, New Territories, Hong Kong. <sup>3</sup>Cardiovascular Research Institute, University of California San Francisco, San Francisco, California, USA. <sup>4</sup>Department of Anatomical and Cellular Pathology, The Chinese University of Hong Kong, Hong Kong. <sup>5</sup>Department of Computer Science, The University of Hong Kong, Hong Kong. <sup>6</sup>BioNano Genomics, San Diego, California, USA. <sup>7</sup>School of Biomedical Engineering, Science and Health Systems, Drexel University, Philadelphia, Pennsylvania, USA. <sup>8</sup>Institute for Human Genetics, University of California San Francisco, San Francisco, California, USA. <sup>9</sup>Hong Kong Bioinformatics Centre. <sup>10</sup>Hong Kong Institute of Diabetes and Obesity. <sup>11</sup>CUHK-BGI Innovation Institute of Trans-omics, The Chinese University of Hong Kong, Hong Kong.

#### References

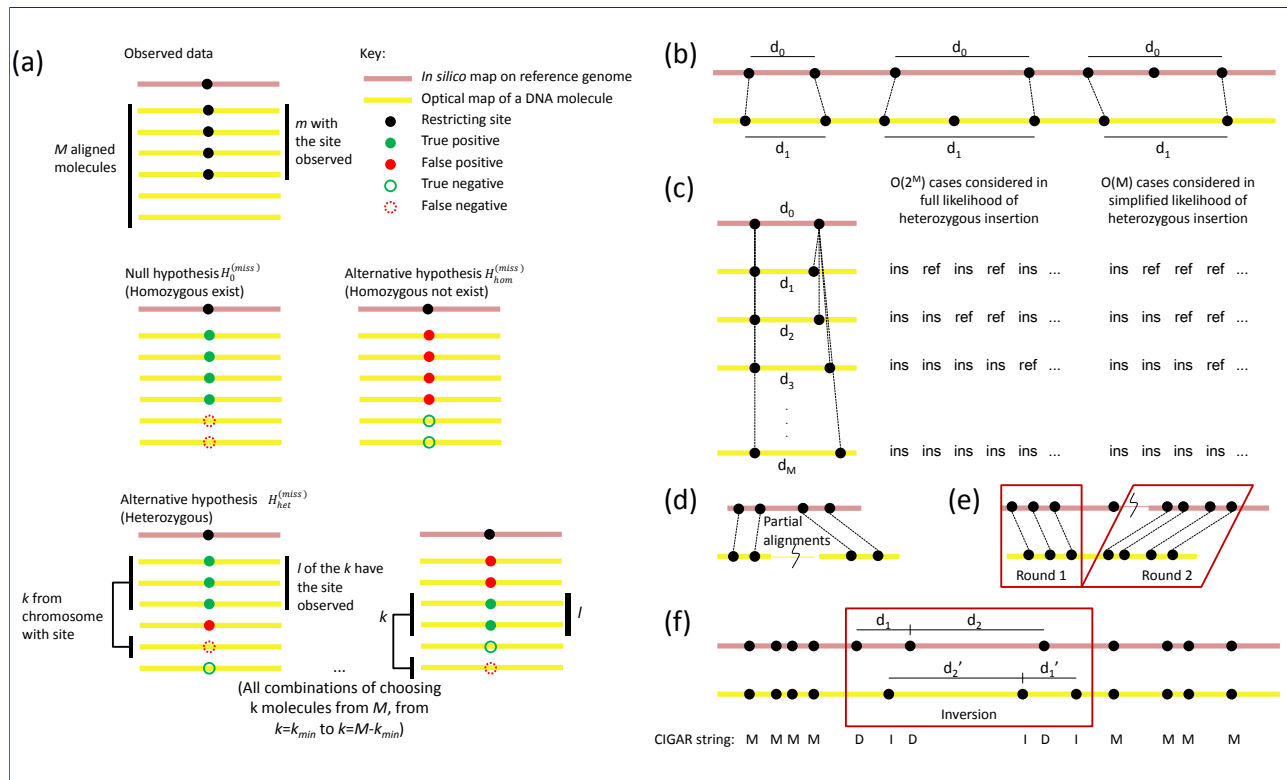
- Feuk, L., Carson, A.R., Scherer, S.W.: Structural variation in the human genome. *Nature Reviews Genetics* **7**, 85–97 (2006)
- Sudmant, P.H., Rausch, T., Gardner, E.J., Handsaker, R.E., Abyzov, A., Huddleston, J., Zhang, Y., Ye, K., Jun, G., Fritz, M.H.-Y., Konkol, M.K., Malhotra, A., Stutz, A.M., Shi, X., Casale, F.P., Chen, J., Hormozdizari, F., Dayama, G., Chen, K., Malig, M., Chaisson, M.J.P., Walter, K., Meiers, S., Kashin, S., Garrison, E., Auton, A., Lam, H.Y.K., Mu, X.J., Alkan, C., Antaki, D., Bae, T., Cerveira, E., Chines, P., Chong, Z., Clarke, L., Dal, E., Ding, L., Emery, S., Fan, X., Gujral, M., Kahveci, F., Kidd, J.M., Kong, Y., Lameijer, E.-W., McCarthy, S., Flicek, P., Gibbs, R.A., Marth, G., Mason, C.E., Menelaou, A., Muzny, D.M., Nelson, B.J., Noor, A., Parrish, N.F., Pendleton, M., Quitadamo, A., Raeder, B., Schadt, E.E., Romanovitch, M., Schlattl, A., Sebra, R., Shabalina, A.A., Untergasser, A., Walker, J.A., Wang, M., Yu, F., Zhang, C., Zhang, J., Zheng-Bradley, X., Zhou, W., Zichner, T., Sebati, J., Batzer, M.A., McCarroll, S.A., Consortium, T.G.P., Mills, R.E., Gerstein, M.B., Bashir, A., Stegle, O., Devine, S.E., Lee, C., Eichler, E.E., Korbelt, J.O.: An integrated map of structural variation in 2,504 human genomes. *Nature* **526**(7571), 75–81 (2015)
- Stankiewicz, P., Lupski, J.R.: Structural variation in the human genome and its role in disease. *Annual Review of Medicine* **61**, 437–455 (2010)
- Weischenfeldt, J., Symmons, O., Spitz, F., Korbelt, J.O.: Phenotypic impact of genomic structural variation: Insights from and for human disease. *Nature Reviews Genetics* **14**(2), 125–138 (2013)
- Li, Y., Zheng, H., Luo, R., Wu, H., Zhu, H., Li, R., Cao, H., Wu, B., Huang, S., Shao, H., Ma, H., Zhang, F., Feng, S., Zhang, W., Du, H., Tian, G., Li, J., Zhang, X., Li, S., Bolund, L., Kristiansen, K., de Smith, A.J., Blakemore, A.I.F., Coin, L.J.M., Yang, H., Wang, J., Wang, J.: Structural variation in two human genomes mapped at single-nucleotide resolution by whole genome de novo assembly. *Nature Biotechnology* **29**(8), 723–730 (2011)
- Alkan, C., Coe, B.P., Eichler, E.E.: Genome structural variation discovery and genotyping. *Nature Reviews Genetics* **12**(5), 363–376 (2011)
- Medvedev, P., Stanciu, M., Brudno, M.: Computational methods for discovering structural variation with next-generation sequencing. *Nature Methods* **6**(11), 13–20 (2009)
- English, A.C., Salerno, W.J., Hampton, O.A., Gonzaga-Jauregui, C., Ambreth, S., Ritter, D.I., Beck, C.R., Davis, C.F., Dahdouli, M., Ma, S., Carroll, A., Veeraraghavan, N., Bruestle, J., Drees, B., Hastie, A., Lam, E.T., White, S., Mishra, P., Wang, M., Han, Y., Zhang, F., Stankiewicz, P., Wheeler, D.A., Reid, J.G., Muzny, D.M., Rogers, J., Sabo, A., Worley, K.C., Lupski, J.R., Boerwinkle, E., Gibbs, R.A.: Assessing structural variation in a personal genome - towards a human reference diploid genome. *BMC Genomics* **16**(286) (2015)
- Zeitouni, B., Boeva, V., Janoueix-Lerosey, I., Loeillet, S., Legoix-ne, P., Nicolas, A., Delattre, O., Barillot, E.: SVDetect: A tool to identify genomic structural variations from paired-end and mate-pair sequencing data. *Bioinformatics* **26**, 1895–1896 (2010)
- Gudbjartsson, D.F., Helgason, H., Gudjonsson, S.A., Zink, F., Oddson, A., Gylfason, A., Besenbacher, S., Magnusson, G., Halldorsson, B.V., Hjartarson, E., Sigurdsson, G.T., Stacey, S.N., Frigge, M.L., Holm, H., Saemundsdottir, J., Helgadóttir, H.T., Johannsdóttir, H., Sigfusson, G., Thorgeirsson, G., Sverrisson, J.T., Gretarsdóttir, S., Walters, G.B., Rafnar, T., Thjodleifsson, B., Bjornsson, E.S., Olafsson, S., Thorarindóttir, H., Steingrimsdóttir, T., Gudmundsdóttir, T.S., Theodors, A., Jonasson, J.G., Sigurdsson, A., Bjornsdóttir, G., Jonsson, J.J., Thorarensen, O., Ludvigsson, P., Gudbjartsson, H., Eyjolfsson, G.I., Sigurdardóttir, O., Olafsson, I., Arnar, D.O., Magnusson, O.T., Kong, A., Masson, G., Thorsteinsdóttir, U., Helgason, A., Sulem, P., Stefansson, K.: Large-scale whole-genome sequencing of the icelandic population. *Nature Genetics* **47**(5), 435–444 (2015)
- Mohiyuddin, M., Mu, J.C., Li, J., Asadi, N.B., Gerstein, M.B., Abyzov, A., Wong, W.H., Lam, H.Y.K.: MetaSV: An accurate and integrative structural-variant caller for next generation sequencing. *Bioinformatics* **31**, 2741–2744 (2015)
- Dimalanta, E.T., Lim, A., Runnheim, R., Lamers, C., Churas, C., Forrest, D.K., de Pablo, J.J., Graham, M.D., Coppersmith, S.N., Goldstein, S., Schwartz, D.C.: A microfluidic system for large DNA molecule arrays. *Analytical Chemistry* **76**, 5293–5301 (2004)
- Lam, E.T., Hastie, A., Lin, C., Ehrlich, D., Das, S.K., Austin, M.D., Deshpande, P., Cao, H., Nagarajan, N., Xiao, M., Kwok, P.-Y.: Genome mapping on nanochannel arrays for structural variation analysis and sequence assembly. *Nature Biotechnology* **30**(8), 771–777 (2012)
- Seo, J.-S., Rhie, A., Kim, J., Lee, S., Sohn, M.-H., Kim, C.-U., Hastie, A., Cao, H., Yun, J.-Y., Kim, J., Kuk, J., Park, G.H., Kim, J., Ryu, H., Kim, J., Roh, M., Baek, J., Hunkapiller, M.W., Korlach, J., Shin, J.-Y., Kim, C.: De novo assembly and phasing of a korean human genome. *Nature* **538**(7624), 243–247 (2016)
- Cao, H., Hastie, A.R., Cao, D., Lam, E.T., Sun, Y., Huang, H., Liu, X., Lin, L., Andrews, W., Chan, S., Huang, S., Tong, X., Requa, M., Anantharaman, T., Krogh, A., Yang, H., Cao, H., Xu, X.: Rapid detection of structural variation in a human genome using nanochannel-based genome mapping technology. *GigaScience* **3**(1), 34 (2014)
- Dong, Y., Xie, M., Jiang, Y., Xiao, N., Du, X., Zhang, W., Tosser-Klopp, G., Wang, J., Yang, S., Liang, J., Chen, W., Chen, J., Zeng, P., Hou, Y., Bian, C., Pan, S., Li, Y., Liu, X., Wang, W., Servin, B., Sayre, B., Zhu, B., Sweeney, D., Moore, R., Nie, W., Shen, Y., Zhao, R., Zhang, G., Li, J., Faraut, T., Womack, J., Zhang, Y., Kijas, J., Cockett, N., Xu, X., Zhao, S., Wang, J., Wang, W.: Sequencing and automated whole-genome optical mapping of the genome of a domestic goat (*capra hircus*). *Nature Biotechnology* **31**(2), 135–141 (2013)
- Ray, M., Goldstein, S., Zhou, S., Potamouisis, K., Sarkar, D., Newton, M.A., Esterberg, E., Kendziorski, C., Bogler, O., Schwartz, D.C.: Discovery of structural alterations in solid tumor oligodendroglioma by single molecule analysis. *BMC Genomics* **14**, 505 (2013)
- Teague, B., Waterman, M.S., Goldstein, S., Potamouisis, K., Zhou, S., Reslewic, S., Sarkar, D., Valouev, A., Churas, C., Kidd, J.M., Kohn, S., Runnheim, R., Lamers, C., Forrest, D., Newton, M.A., Eichler, E.E., Kent-First, M., Surti, U., Livny, M., Schwartz, D.C.: High-resolution human genome structure by single-molecule analysis.

- Proceedings of the National Academy of Sciences of the United States of America **107**(24), 10848–10853 (2010)
19. Tong, L.: Bayesian methods in multi-color optical mapping. *International Journal of Mathematics and Computer Science* **5**, 101–122 (2010)
  20. Valouev, A., Zhang, Y., Schwartz, D.C., Waterman, M.S.: Refinement of optical map assemblies. *Bioinformatics* **22**(10), 1217–1224 (2006)
  21. Tong, L., Mets, L., McPeck, M.S.: Likelihood-based inference for multi-color optical mapping. *Statistical Applications in Genetics and Molecular Biology* **6**, 5 (2007)
  22. Leung, A.K.-Y., Kwok, T.-P., Wan, R., Xiao, M., Kwok, P.-Y., Yip, K.Y., Chan, T.-F.: OMBlast: Alignment tool for optical mapping using a seed-and-extend approach. *Bioinformatics* **33**, 311–319 (2017)
  23. Nagarajan, N., Read, T.D., Pop, M.: Scaffolding and validation of bacterial genome assemblies using optical restriction maps. *Bioinformatics* **24**(10), 1229–1235 (2008)
  24. Shelton, J.M., Coleman, M.C., Herndon, N., Lu, N., Lam, E.T., Anantharaman, T., Sheth, P., Brown, S.J.: Tools and pipelines for BioNano data: Molecule assembly pipeline and FASTA super scaffolding tool. *BMC Genomics* **16**, 734 (2015)
  25. Kim, J., Larkin, D.M., Cai, Q., Asan, Zhang, Y., Ge, R.-L., Auvil, L., Capitanu, B., Zhang, G., Lewin, H.A., Ma, J.: Reference-assisted chromosome assembly. *Proceedings of the National Academy of Sciences of the United States of America* **110**(5), 1785–1790 (2013)
  26. Lin, H.C., Goldstein, S., Mendelowitz, L., Zhou, S., Wetzel, J., Schwartz, D.C., Pop, M.: AGORA: Assembly guided by optical restriction alignment. *BMC Bioinformatics* **13**, 189 (2012)
  27. Hastie, A.R., Dong, L., Smith, A., Finklestein, J., Lam, E.T., Huo, N., Cao, H., Kwok, P.-Y., Deal, K.R., Dvorak, J., Luo, M.-C., Gu, Y., Xiao, M.: Rapid genome mapping in nanochannel arrays for highly complete and accurate de novo sequence assembly of the complex *aegilops tauschii* genome. *PLOS ONE* **8**(2), 55864 (2013)
  28. Mak, A.C.Y., Lai, Y.Y.Y., Lam, E.T., Kwok, T.-P., Leung, A.K.Y., Poon, A., Mostovoy, Y., Hastie, A.R., Stedman, W., Anantharaman, T., Andrews, W., Zhou, X., Pang, A.W.C., Dai, H., Chu, C., Lin, C., Wu, J.J.K., Li, C.M.L., Li, J.-W., Yim, A.K.Y., Chan, S., Sibert, J., Dzakula, Z., Cao, H., Yiu, S.-M., Chan, T.-F., Yip, K.Y., Xiao, M., Kwok, P.-Y.: Genome-wide structural variation detection by genome mapping on nanochannel arrays. *Genetics* **202**(1), 351–362 (2016)
  29. MacDonald, J.R., Ziman, R., Yuen, R.K.C., Feuk, L., Scherer, S.W.: The database of genomic variants: A curated collection of structural variation in the human genome. *Nucleic Acids Research* **42**, 986–992 (2014)
  30. Parikh, H., Mohiyuddin, M., Lam, H.Y., Iyer, H., Chen, D., Pratt, M., Bartha, G., Spies, N., Losert, W., Zook, J.M., Salit, M.: svclassify: A method to establish benchmark structural variant calls. *BMC Genomics* **17**(1), 64 (2016)
  31. Cheung, S.T., Huang, D.P., Hui, A.B.Y., Lo, K.W., Ko, C.W., Tsang, Y.S., Wong, N., Whitney, B.M., Lee, J.C.K.: Nasopharyngeal carcinoma cell line (C666-1) consistently harbouring Epstein-Barr virus. *International Journal of Cancer* **83**, 121–126 (1999)
  32. Tso, K.K.-Y., Yip, K.Y., Mak, C., Chung, G.T.-Y., Lee, S.-D., Cheung, S.-T., To, K.-F., Lo, K.-W.: Complete genomic sequence of Epstein-Barr virus in nasopharyngeal carcinoma cell line C666-1. *Infectious Agents and Cancer* **8**, 29 (2013)
  33. Xiao, K., Yu, Z., Li, X., Li, X., Tang, K., Tu, C., Qi, P., Liao, Q., Chen, P., Zeng, Z., Li, G., Xiong, W.: Genome-wide analysis of Epstein-Barr virus (EBV) integration and strain in c666-1 and raji cells. *Journal of Cancer* **7**, 214–224 (2016)
  34. Bailey, J.A., Yavor, A.M., Massa, H.F., Trask, B.J., Eichler, E.E.: Segmental duplications: Organization and impact within the current human genome project assembly. *Genome Research* **11**, 1005–1017 (2001)
  35. Bailey, J.A., Gu, Z., Clark, R.A., Reinert, K., Samonte, R.V., Schwartz, S., Adams, M.D., Myers, E.W., Li, P.W., Eichler, E.E.: Recent segmental duplications in the human genome. *Science* **297**(5583), 1003–1007 (2002)
  36. Chung, G.T.-Y., Lung, R.W.-M., Hui, A.B.-Y., Yip, K.Y.-L., Woo, J.K.-S., Chow, C., Tong, C.Y.-K., Lee, S.-D., Yuen, J.W.-F., Lun, S.W.-M., Tso, K.K.-Y., Wong, N., Tsao, S.-W., Yip, T.T.-C., Busson, P., Kim, H., Seo, J.-S., O'Sullivan, B., Liu, F.-F., To, K.-F., Lo, K.-W.: Identification of a recurrent transforming UBR5–ZNF423 fusion gene in EBV-associated nasopharyngeal carcinoma. *The Journal of Pathology* **231**(2), 158–167 (2013)
  37. Chen, X., Schulz-Trieglaff, O., Shaw, R., Barnes, B., Schlesinger, F., Kallberg, M., Cox, A.J., Kruglyak, S., Saunders, C.T.: Manta: Rapid detection of structural variants and indels for germline and cancer sequencing applications. *Bioinformatics* **32**, 1220–1222 (2016)
  38. Ye, K., Schulz, M.H., Long, Q., Apweiler, R., Ning, Z.: Pindel: A pattern growth approach to detect break points of large deletions and medium sized insertions from paired-end short reads. *Bioinformatics* **25**, 2865–2871 (2009)
  39. Hanson, K.M., Wolf, D.R.: Estimators for the cauchy distribution. In: *Proceedings of the Fifteenth International Workshop on Maximum Entropy and Bayesian Methods*, pp. 255–263 (1996)
  40. Yoon, S., Xuan, Z., Makarov, V., Ye, K., Sebat, J.: Sensitive and accurate detection of copy number variants using read depth of coverage. *Genome research* **19**(9), 1586–1592 (2009)
  41. Kent, W.J., Sugnet, C.W., Furey, T.S., Roskin, K.M., Pringle, T.H., Zahler, A.M., Haussler, D.: The human genome browser at UCSC. *Genome Research* **12**, 996–1006 (2002)
  42. Hu, X., Yuan, J., Shi, Y., Lu, J., Liu, B., Li, Z., Chen, Y., Mu, D., Zhang, H., Li, N., Yue, Z., Bai, F., Li, H., Fan, W.: pIRS: Profile-based illumina pair-end reads simulator. *Bioinformatics* **28**(11), 1533–1535 (2012)
  43. The 1000 Genomes Project Consortium: A map of human genome variation from population-scale sequencing. *Nature* **467**(7319), 1061–1073 (2010)
  44. Lu, J.T., Wang, Y., Gibbs, R.A., Yu, F.: Characterizing linkage disequilibrium and evaluating imputation power of human genomic insertion-deletion polymorphisms. *Genome Biology* **13**(R15) (2012)
  45. Pang, A.W., MacDonald, J.R., Pinto, D., Wei, J., Rafiq, M.A., Conrad, D.F., Park, H., Hurler, M.E., Lee, C., Venter, J.C., Kirkness, E.F., Levy, S., Feuk, L., Scherer, S.W.: Towards a comprehensive structural variation map of an individual human genome. *Genome Biology* **11**(R52) (2010)
  46. Levy, S., Sutton, G., Ng, P.C., Feuk, L., Halpern, A.L., Walenz, B.P., Axelrod, N., Huang, J., Kirkness, E.F., Denisov, G., Lin, Y., MacDonald, J.R., Pang, A.W.C., Shago, M., Stockwell, T.B., Tsiamouri, A., Bafna, V., Bansal, V., Kravitz, S.A., Busam, D.A., Beeson, K.Y., McIntosh, T.C., Remington, K.A., Abril, J.F., Gill, J., Borman, J., Rogers, Y.-H., Frazier, M.E., Scherer, S.W., Strausberg, R.L., Venter, J.C.: The diploid genome sequence of an individual human. *PLOS Biology* **5**(e254) (2007)
  47. Luo, R., Liu, B., Xie, Y., Li, Z., Huang, W., Yuan, J., He, G., Chen, Y., Pan, Q., Liu, Y., Tang, J., Wu, G., Zhang, H., Shi, Y., Liu, Y., Yu, C., Wang, B., Lu, Y., Han, C., Cheung, D.W., Yiu, S.-M., Peng, S., Xiaoqian, Z., Liu, G., Liao, X., Li, Y., Yang, H., Wang, J., Lam, T.-W., Wang, J.: SOAPdenovo2: An empirically improved memory-efficient short-read de novo assembler. *GigaScience* **1**, 18 (2012)
  48. Li, H., Durbin, R.: Fast and accurate short read alignment with burrowswheeler transform. *Bioinformatics* **25**, 1754–1760 (2009)
  49. Robinson, J.T., Thorvaldsdottir, H., Winckler, W., Guttman, M., Lander, E.S., Getz, G., Mesirov, J.P.: Integrative genomics viewer. *Nature Biotechnology* **29**(1), 24–26 (2011)
  50. Leung, A.K.-Y., Jin, N., Yip, K.Y., Chan, T.-F.: OMTools: A software package for visualizing and processing optical mapping data. *Bioinformatics* **33**, 2933–2935 (2017)
  51. Gupta, A., Place, M., Goldstein, S., Sarkar, D., Zhou, S., Potamoumis, K., Kim, J., Flanagan, C., Li, Y., Newton, M.A., Callander, N.S., Dematti, P., Bresnick, E.H., Ma, J., Asimakopoulos, F., Schwartz, D.C.: Single-molecule analysis reveals widespread structural variation in multiple myeloma. *Proceedings of the National Academy of Sciences of the United States of America* **112**(25), 7689–7694 (2015)

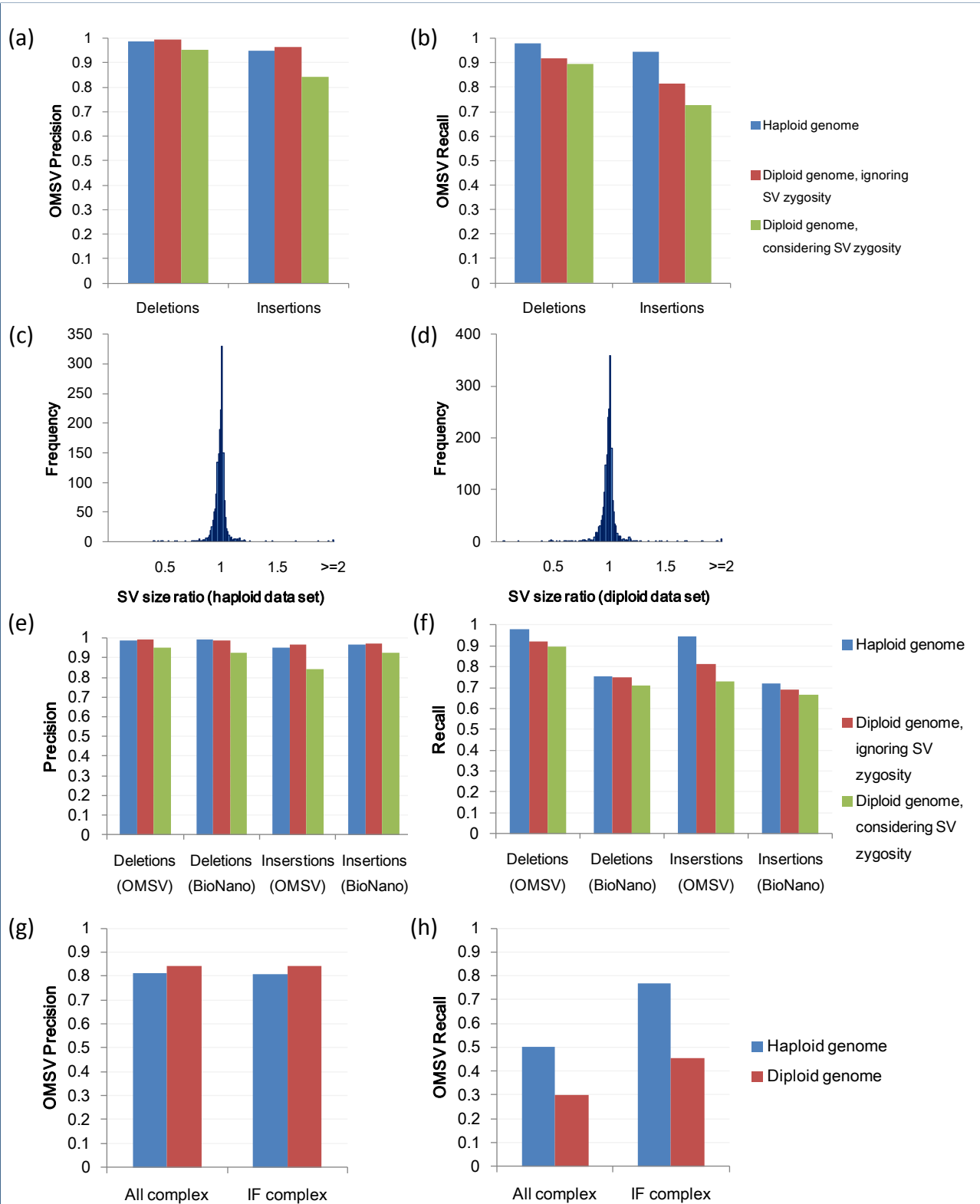
Figures



**Figure 1** Underlying concepts of OMSV. (a) Different types of genetic variations and their idealized appearance patterns on optical maps. Real OM data contain various types of errors that make these patterns less apparent. Inversions are shown as an example type of complex SVs, while OMSV can also detect translocations and copy number variations. (b) The overall OMSV pipeline for identifying SVs from optical maps. Optical maps from a study sample are aligned to the reference map using two different aligners. Their results are integrated to form a single list of consensus alignments, which are then passed to three SV calling modules to identify different types of SVs.

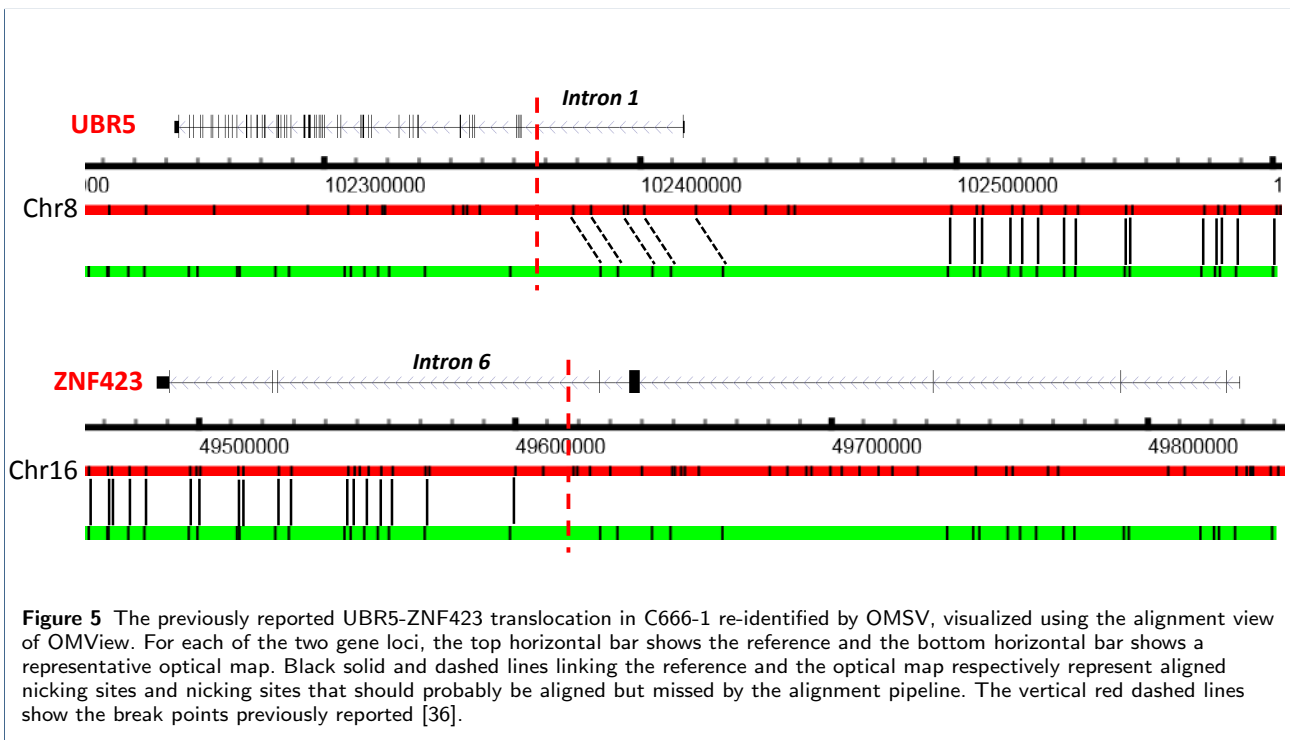


**Figure 2** Illustration of methods used by OMSV for identifying SVs from optical maps. (a) The three hypotheses compared in the procedure for detecting missing restriction sites. (b) Comparing the distance between two restriction sites on the reference and the corresponding observed labels on the optical maps, for detecting large SVs. (c) Simplification of the likelihood function for the heterozygous insertion hypothesis. In the full likelihood function, each optical map could come from the chromosome with the reference allele (ref) or the insertion allele (ins), and all combinations are considered. In the simplified likelihood function, only the  $k$  optical maps with the largest distance between the two nicking site labels are considered to have the insertion, and all values of  $k$  are considered. In this illustration, the minimum number of optical maps supporting each allele,  $k_{min}$ , is set to 0. (d) SVs that require partial alignments to identify. (e) Translocations and large inversions can be identified by 2-round split alignments. (f) Medium-size inversions are identified by looking for regions with a reverse palindromic CIGAR string (DIDIDI in this example) with matched segment sizes when reversed ( $d_1$  with  $d'_1$  and  $d_2$  with  $d'_2$  in this example).



**Figure 3** Results based on the default simulated data sets. Precision (a) and recall (b) of OMSV. Ratio of SV sizes determined by OMSV to their actual sizes, for the haploid (c) and diploid (d) data sets. Precision (e) and recall (f) of OMSV as compared to BioNano Solve. Results in Panels (a) to (f) are all based on insertions and deletions larger than 2kbp. Precision (g) and recall (h) of OMSV in calling complex SVs from the simulated data, including the whole set (“All”) and only the intrinsically feasible (“IF”) ones.





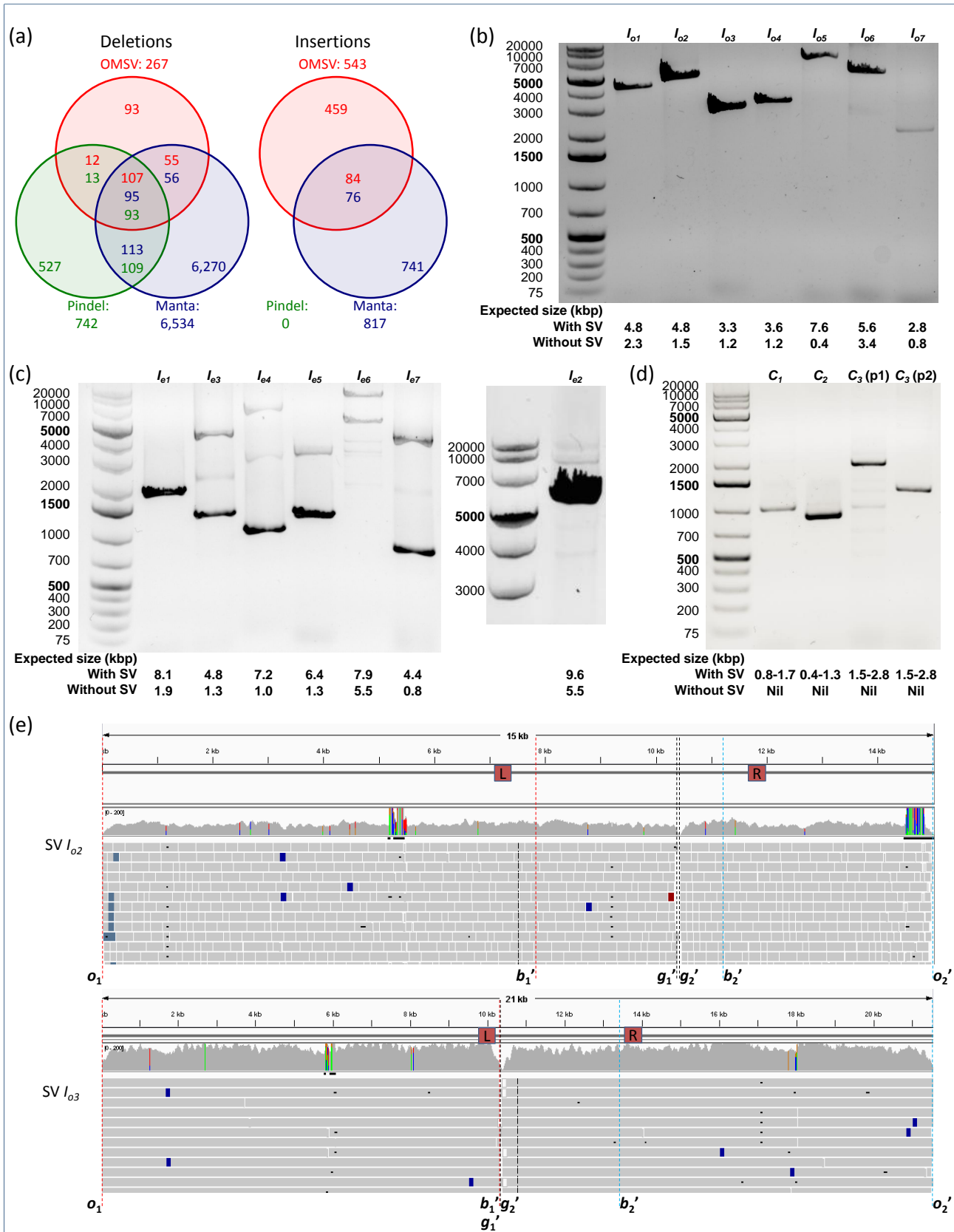


**Figure 6** SVs identified by OMSV from C666-1. (a) Overlap between the large (>2kbp) indels identified by OMSV and the two short-read based callers, Manta and Pindel. In the common regions, the number of a certain color indicates the number of SVs called by the respective method that overlap SVs called by the other method(s). (b-d) PCR results of the selected homozygous insertions (b), heterozygous insertions (c) and complex SVs (d). In the heterozygous insertions,  $I_{e2}$  was tested separately from the other 6 cases due to the large expected product size of its insertion allele. For the inversion case  $C_3$ , p1 and p2 correspond to the two primer pairs. (e) Alignment of sequencing reads to the inferred C666-1 sequences of SV  $I_{o2}$  and SV  $I_{o3}$ . The L and R boxes mark the primer locations. Definitions of  $o_1$ ,  $o_2$ ,  $b_1'$ ,  $b_2'$ ,  $g_1'$  and  $g_2'$  are given in Additional file 1: Figure S9. Sequencing read alignments are visualized by IGV.

**Additional Files**

## Additional file 1 – Supplementary tables and figures

Containing Supplementary Tables S1–S16 and Supplementary Figures S1–S11

## Additional file 7 — Gaps in hg38

This file provides the locations of unspecified nucleotides ('N's) in the human reference genome hg38.

## Additional file 8 — Pseudo-autosomal regions in hg38

This file provides the locations of pseudo-autosomal regions in the human reference genome hg38.

## Additional file 2 — SV lists from the CEU trio

This file provides the SVs identified by OMSV from the CEU trio. The first three sheets list the indels identified from NA12878, NA12891 and NA12892, respectively. The fourth sheet lists the union of these three lists. The fifth sheet lists all the sites with multiple indels called at the same site (two insertions, two deletions, or one insertion and one deletion). The sixth sheet lists the high-confidence indels and non-indels for evaluating Mendelian concordance. The last sheet lists the complex SVs.

## Additional file 3 — SV list from the C666-1 cell line

This file provides the SVs identified by OMSV from the C666-1 cell line. The first sheet lists the indels identified. The second sheet lists all the sites with multiple indels called at the same site (two insertions, two deletions, or one insertion and one deletion). The third sheet lists the complex SVs.

## Additional file 4 — Overlapping of C666-1 indels with segmental duplications

This file provides the overlap of C666-1 indels identified by OMSV with human segmental duplications. The first three columns show the genomic location of the SVs. The fourth column shows the SV type. The fifth and sixth columns show the overlapping segmental duplications (if any) and the genes of which the exons overlap the segmental duplications (if any).

## Additional file 5 — Case studies of complex SVs of C666-1

This file provides visualizations of selected cases of complex SVs identified by OMSV from C666-1.

Additional file 6 — Fragile sites in the *in silico* map based on hg38

This file provides the locations of fragile sites in the human reference genome hg38.

## Supplementary tables

Publication	SV types supported	Zygoty call?	Assembly-based?	Software availability
Teague et al. (2010) [18]	Indels	No	Yes	Not publicly available
Ray et al. (2013) [17]	Indels	No	Yes	Not publicly available
Cao et al. (2014) [15]	Indels/inversions	No	Yes	Predecessor of BioNano Solve
Gupta et al. (2015) [51]	Indels	No	Yes	Not publicly available
Mak et al. (2016) [28]	Indels/inversions	No	Yes, also a module based on alignment	Predecessors of BioNano Solve and OMSV

**Table S1** Existing SV calling methods based on optical mapping.

Genome	Optical maps generated	Genome coverage	FP	FN	Avg. optical map length (bp)	Avg. nicking sites per map	Density of nicking sites (per Mbp)	Optical maps aligned	Alignment rate
Haploid	1,500,000	100	1.2E-5	1.2E-1	200,780	22.9	114.0	1,203,728	80.2%
Diploid	1,500,000	100	1.2E-5	1.2E-1	200,814	22.9	114.0	1,214,539	81.0%
Diploid	300,000	20	1.2E-5	1.2E-1	200,622	22.9	114.1	243,006	81.0%
Diploid	500,000	33	1.2E-5	1.2E-1	200,576	22.9	114.1	404,805	81.0%
Diploid	700,000	47	1.2E-5	1.2E-1	200,681	22.9	114.1	566,912	81.0%
Diploid	900,000	60	1.2E-5	1.2E-1	200,679	22.9	114.1	728,672	81.0%
Diploid	1,100,000	73	1.2E-5	1.2E-1	200,771	22.9	114.0	890,816	81.0%
Diploid	1,300,000	87	1.2E-5	1.2E-1	200,796	22.9	114.0	1,052,735	81.0%
Diploid	1,700,000	113	1.2E-5	1.2E-1	200,820	22.9	114.0	1,376,494	81.0%
Diploid	1,900,000	127	1.2E-5	1.2E-1	200,793	22.9	114.0	1,538,631	81.0%
Diploid	2,100,000	140	1.2E-5	1.2E-1	200,812	22.9	114.0	1,700,717	81.0%
Diploid	2,300,000	153	1.2E-5	1.2E-1	200,820	22.9	114.0	1,862,534	81.0%
Diploid	2,500,000	167	1.2E-5	1.2E-1	200,786	22.9	114.0	2,024,415	81.0%
Diploid	1,500,000	100	0	1.2E-1	200,713	20.9	104.1	1,282,369	85.5%
Diploid	1,500,000	100	1.2E-8	1.2E-1	200,791	20.9	104.1	1,282,268	85.5%
Diploid	1,500,000	100	1.2E-7	1.2E-1	200,806	20.9	104.1	1,281,988	85.5%
Diploid	1,500,000	100	1.2E-6	1.2E-1	200,785	21.1	105.1	1,276,595	85.1%
Diploid	1,500,000	100	3.0E-5	1.2E-1	200,772	25.9	129.0	1,096,354	73.1%
Diploid	1,500,000	100	6.0E-5	1.2E-1	200,801	30.7	152.9	1,018,500	67.9%
Diploid	1,500,000	100	9.0E-5	1.2E-1	200,834	35.3	175.8	1,303,880	86.9%
Diploid	1,500,000	100	1.2E-4	1.2E-1	200,816	39.6	197.2	1,366,980	91.1%
Diploid	1,500,000	100	1.2E-5	0	200,538	25.3	126.2	1,309,947	87.3%
Diploid	1,500,000	100	1.2E-5	1.2E-4	200,525	25.3	126.2	1,310,001	87.3%
Diploid	1,500,000	100	1.2E-5	1.2E-3	200,564	25.3	126.2	1,309,055	87.3%
Diploid	1,500,000	100	1.2E-5	1.2E-2	200,564	25.1	125.1	1,303,178	86.9%
Diploid	1,500,000	100	1.2E-5	2.4E-1	201,321	20.5	101.8	1,037,081	69.1%
Diploid	1,500,000	100	1.2E-5	3.6E-1	202,626	18.0	88.8	768,478	51.2%
Diploid	1,500,000	100	1.2E-5	4.8E-1	205,510	15.7	76.4	444,795	29.7%

**Table S2** Statistics of the simulated optical maps. FP and FN refer to the rates for a fake nicking site to be observed and a real nicking site to be unobserved, respectively. The first two rows show the statistics of the haploid and diploid data sets based on the default setting, and the other rows show the settings with different genome coverage, FP and FN values.

Genome	Homozygous insertions	Homozygous deletions	Heterozygous insertions	Heterozygous deletions	Complex	Total
Haploid	936	911	0	0	983	2830
Diploid	485	467	451	444	983	2830

**Table S3** Statistics of SVs in the simulated data sets. All 27 diploid data sets listed in Table S2 were generated based on the same diploid genome with the SV profile shown here. The number of complex SVs generated is larger than that of a typical human sample, to test OMSV's ability to identify complex SVs.

Step	Time needed (hours)	
	Haploid genome	Diploid genome
OMBlast alignment (using 1 thread)	225	225
OMBlast alignment (using 64 threads)	3.47	3.52
RefAligner alignment (using 1 thread)	49	50
RefAligner alignment (using 64 threads)	0.77	0.79
SV calling (using 1 thread)	1.24	1.24
Total (using 1 thread)	226	226
Total (using 64 threads)	4.71	4.76

**Table S4** Running time of OMSV on simulated data with 100x coverage of the human genome. The total amount of time is defined as the maximum time for the two alignment methods plus the time for SV calling.

Samples	Optical maps generated	Avg. optical map length (bp)	Avg. nicking sites per map	Density of nicking sites (per Mbp)	Optical maps aligned	Alignment rate
NA12878	1,540,247	207,926	22.5	108.2	1,264,390	82.1%
NA12891	1,481,578	214,366	24.4	113.8	1,205,487	81.4%
NA12892	2,065,938	184,264	19.8	107.5	1,641,813	79.5%

**Table S5** Statistics of the optical maps produced from the family trio.

Sample	SV type	On autosomes	On sex chromosomes*	X error	Y error
NA12878 (daughter)	Insertion	538	27	N/A	0
	Deletion	523	25	N/A	0
	Multiple	8	1	N/A	0
	CNV	29	1	N/A	0
	Medium Inversion	30	0	N/A	0
	Large Inversion	22	5	N/A	0
	Intra-chromosomal Translocation	1	0	N/A	0
	Inter-chromosomal Translocation	1	0	N/A	0
	Total	1,152	59	N/A	0
	NA12891 (father)	Insertion	573	31	7
Deletion		500	22	8	1
Multiple		7	0	N/A	N/A
CNV		22	6	N/A	N/A
Medium Inversion		27	1	N/A	N/A
Large Inversion		25	4	N/A	N/A
Intra-chromosomal Translocation		0	0	N/A	N/A
Inter-chromosomal Translocation		1	0	N/A	N/A
Total		1,155	64	15	3
NA12892 (mother)		Insertion	536	20	N/A
	Deletion	477	21	N/A	0
	Multiple	6	0	N/A	N/A
	CNV	45	3	N/A	N/A
	Medium Inversion	21	0	N/A	N/A
	Large Inversion	31	6	N/A	N/A
	Intra-chromosomal Translocation	2	0	N/A	N/A
	Inter-chromosomal Translocation	45	5	N/A	N/A
	Total	1,163	55	N/A	3

**Table S6** Statistics of SVs called from the optical maps produced from each member of the trio. The "Multiple" SV type corresponds to a locus with multiple indels called at the same site (two insertions, two deletions, or one insertion and one deletion). These cases are not included in the counts of the "Insertion" and "Deletion" cases. X error includes SVs called in the non-pseudo-autosomal regions of the X chromosome as heterozygous from a male sample. Y error includes SVs called in the non-pseudo-autosomal regions of the Y chromosome either from a female sample or in heterozygous form from a male sample. Since OMSV does not determine the zygosity of complex SVs, they were not included in the calculation of X and Y errors that involved zygosity. An inter-chromosomal translocation is counted as appearing on a sex chromosome if either of the two chromosomes involved is a sex chromosome. \*Pseudo-autosomal regions are excluded.

Sample	Total number of SVs called	Intersection with manual checking list	Validated by manual checking		Validation rate	
			Ignoring zygosity	Considering zygosity	Ignoring zygosity	Considering zygosity
NA12878	991	726	705	527	0.97	0.73
NA12891	1007	696	669	516	0.96	0.74
NA12892	926	642	615	471	0.96	0.73

**Table S7** Accuracy of the SVs called by OMSV based on the manual checking results in Mak et al. The SVs from the three individuals were integrated and de-duplicated, and then the SVs contained in each individual were extracted from the resulting list, before comparing with the manual checking results.

Optical maps generated	Avg. optical map length (bp)	Avg. nicking sites per map	Density of nicking sites (per Mbp)	Optical maps aligned	Alignment rate
1,644,102	244,075	22.8	93.4	1,129,075	68.7%

**Table S8** Statistics of the optical maps produced from the C666-1 cell line.

Sample	SV type	On autosomes	On sex chromosomes*	X error	Y error
C666-1 (male)	Insertion	527	16	6	0
	Deletion	262	5	0	0
	Multiple	3	0	N/A	N/A
	CNV	66	2	N/A	N/A
	Medium inversion	24	4	N/A	N/A
	Large inversion	10	3	N/A	N/A
	Intra-chromosomal translocation	2	0	N/A	N/A
	Inter-chromosomal translocation	4	0	N/A	N/A
	Total	898	30	6	0

**Table S9** Statistics of SVs called from the C666-1 cell line optical maps. The “Multiple” SV type corresponds to a locus with multiple indels called at the same site (two insertions, two deletions, or one insertion and one deletion). These cases are not included in the counts of the “Insertion” and “Deletion” cases. X error and Y error respectively includes SVs called in the non-pseudo-autosomal regions of the X and Y chromosome as heterozygous. Since OMSV does not determine the zygosity of complex SVs, they were not included in the calculation of X and Y errors. An inter-chromosomal translocation is counted as appearing on a sex chromosome if either of the two chromosomes involved is a sex chromosome. \*Pseudo-autosomal regions are excluded.

SV ID	$I_{o1}$	$I_{o2}$	$I_{o3}$	$I_{o4}$	$I_{o5}$	$I_{o6}$	$I_{o7}$
Chr	1	3	8	12	14	15	16
$o_1$	10,969,439	154,172,724	21,505,975	40,144,059	104,496,071	74,214,211	86,985,730
$o_2$	10,971,543	154,184,477	21,525,476	40,149,705	104,499,324	74,220,313	86,988,880
$s$	2,501	3,273	2,050	2,405	7,222	2,217	2,012
Primer location							
Left primer	10,969,341-10,969,363	154,179,761-154,179,783	21,516,348-21,516,372	40,145,694-40,145,715	104,498,683-104,498,705	74,215,116-74,215,138	86,986,707-86,986,727
Right primer	10,971,633-10,971,656	154,181,240-154,181,263	21,517,547-21,517,570	40,146,848-40,146,870	104,499,061-104,499,084	74,218,504-74,218,526	86,987,474-86,987,496
Predicted PCR product size							
With SV	4,817	4,776	3,273	3,562	7,624	5,628	2,780
Without SV	2,316	1,503	1,223	1,157	402	3,411	768
Detected by sequencing-based SV caller?							
Manta	Yes	Yes	No	No	No	Yes	No
Pindel	No	No	No	No	No	No	No
$b_1$	10,971,095-	154,180,619-	21,516,373-	40,145,895-	104,498,838-	74,216,616-	86,986,874-
$b_2$	10,971,077	154,180,621	21,517,291	40,146,766	104,498,911	74,216,611	86,986,968

**Table S10** List of homozygous insertions identified by OMSV from C666-1 that underwent experimental validations. Definitions of  $o_1$ ,  $o_2$ ,  $s$ ,  $b_1$  and  $b_2$  are given in Figure S9. PCR product sizes were predicted by considering both primer locations and insertion size  $s$  determined by OMSV.

SV ID	$I_{e1}$	$I_{e2}$	$I_{e3}$	$I_{e4}$	$I_{e5}$	$I_{e6}$	$I_{e7}$
Chr	2	4	5	5	20	1	4
$o_1$	22,961,852	37,948,238	9,967,483	137,676,345	61,555,087	223,473,487	96,500,882
$o_2$	22,969,321	37,960,828	9,972,346	137,689,062	61,561,856	223,487,948	96,507,004
$s$	6,190	4,085	3,496	4,904	5,069	2,428	3,620
Primer location							
Left primer	22,961,879-22,961,901	37,949,749-37,949,772	9,970,229-9,970,251	137,678,394-137,678,415	61,560,697-61,560,717	223,474,377-223,474,399	96,501,977-96,502,001
Right primer	22,963,770-22,963,792	37,955,267-37,955,289	9,971,538-9,971,560	137,679,399-137,679,421	61,561,964-61,561,985	223,479,822-223,479,844	96,502,754-96,502,777
Predicted PCR product size							
With SV	8,104	9,626	4,828	7,232*	6,358	7,896	4,421
Without SV	1,914	5,541	1,332	1,028	1,289	5,468	801
Detected by sequencing-based SV caller?							
Manta	No	Yes (het.)	Yes (het.)	Yes (het.)	No	No	Yes (het.)
Pindel	No	No	No	No	No	No	No
$b_1$	22,962,381-	37,950,488-	9,971,225-	137,682,429-	61,559,538-	Unable to infer	Unable to infer
$b_2$	22,962,381	37,950,488	9,971,225	137,682,429	61,559,499	Unable to infer	Unable to infer

**Table S11** List of heterozygous insertions identified by OMSV from C666-1 that underwent experimental validations. Definitions of  $o_1$ ,  $o_2$ ,  $s$ ,  $b_1$  and  $b_2$  are given in Figure S9. PCR product sizes were predicted by considering both primer locations and insertion size  $s$  determined by OMSV. In the Manta predictions, het. denotes that the SV was predicted to be heterozygous. \*The predicted PCR product size of  $I_{e4}$  is not equal to the summation of the size without SV and  $s$ , because GapCloser’s result reveals an extra deletion of around 1,300bp between  $o_1$  and  $o_2$  but outside the designed primer pair. As a result, the expected PCR product size without the SV is not affected (since the deletion is outside the primer pair) and is equal to the span of the genomic region covered by the two primers, but the estimated insertion size  $s$  should be increased by 1,300bp since it was originally inferred by OMSV without knowing that the two defining nicking sites were actually 1,300bp closer to each other in C666-1 as compared to the reference genome.

SV ID	$C_1$	$C_2$	$C_3$
Type	Inter-trans.	Intra-trans.	Inversion
Chr 1st	5	8	X
$o_1$	77,697,732	22,574,642	149,634,449
Translocated segment 1st	left of $o_1$	left of $o_1$	
Chr 2nd	8	8	X
$o_2$	27,323,114	30,293,029	149,727,161
Translocated segment 2nd	left of $o_2$	right of $o_2$	
Primer location			
Primer pair 1			
Left primer	chr5:77,933,545- chr5:77,933,567	22,570,830- 22,570,852	149,652,660- 149,652,682
Right primer	chr8:27,559,009- chr8:27,559,031	30,262,222- 30,262,244	149,748,923- 149,748,945
Primer pair 2 (for inversions)			
Left primer			149,654,409- 149,654,431
Right primer			149,750,609- 149,750,631
Predicted PCR product size			
Primer pair 1			
With SV	800-1,700	400-1,300	1,500-2,800
Without SV	No product	No product	No product
Primer pair 2 (for inversions)			
With SV			1,500-2,800
Without SV			No product
Detected by sequencing-based SV caller?			
Manta	Yes	Yes (Del.)	No
Pindel	No	No	No
$b_{11}$	chr5:77,934,208-	22,571,087-	149,653,932-
$b_{12}$	chr5:77,934,308	22,571,287	149,654,132
$b_{21}$	chr8:27,559,341-	30,261,884-	149,748,939-
$b_{22}$	chr8:27,559,441	30,261,984	149,749,439

**Table S12** List of complex SVs identified by OMSV from C666-1 that underwent experimental validations. Inter-trans. and Intra-trans. refer to inter-chromosomal translocation and intra-chromosomal translocation, respectively. Chr 1st and Chr 2nd are the chromosomes of the first and second break points, which are different for inter-chromosomal translocations. Definitions of  $o_1$  and  $o_2$  and locations of the break points estimated by OMSV.  $[b_{11}, b_{12}]$  and  $[b_{21}, b_{22}]$  are the approximate break point locations estimated by sequencing reads. PCR product sizes were predicted by considering both the distance between the defining nicking sites and the locations of the designed primers. In the Manta predictions, del. denotes that the SV was predicted to be a deletion.

SV ID	Primer	Primer sequence
$I_{o1}$	Left	GACATCCAATGCTTTCCTACTCC
	Right	TCAAGTCAGGAAGGAAAGAGACAC
$I_{o2}$	Left	TGGATGTTGGTTACTGGGAATGG
	Right	CCAGATAAGTGGCAGCGAAGTATG
$I_{o3}$	Left	CAGGCAGTCTGGATGCATTGTAC
	Right	GTGACTTGCCTGATCAACAGAATG
$I_{o4}$	Left	CAAGGTGAAACCCCGTCTCTAC
	Right	GTTGTCTCTTGTGTTGAACTGC
$I_{o5}$	Left	AAAAGGGATTCTCACACTCTCGG
	Right	AGATCAGTATTCAGGCTCAGTGTG
$I_{o6}$	Left	TAGCCAGTCTGCAGGATGAGTAG
	Right	CATCATGCTGCCCGTCATTCTTG
$I_{o7}$	Left	GTAAGTGTGCTATTGGCTGTG
	Right	GGACTGGTTAAATGGTGATTAGG
$I_{e1}$	Left	TTACCTGAGACACATAGACTGGG
	Right	TGGTAGCCAGACTGTAATAGG
$I_{e2}$	Left	ATGTAGCAACTATTCAACTCTGCC
	Right	GGAATCTCTCATTAAGTCTGCG
$I_{e3}$	Left	AACAGCCCAACAACCTCTATAGG
	Right	TAGCAGTGTGTGAGATACCAGC
$I_{e4}$	Left	GGCCATCATCCTGCTATTAGAG
	Right	CAGAGATGTTGGTGCTGGTTTGC
$I_{e5}$	Left	TTAGCTTCCAGGAACGTGAGC
	Right	GAAGGTCCCTCTCTCTCTGG
$I_{e6}$	Left	AGAGGGAAAGAAGGAAGGGAAGC
	Right	TGTTAAAGCTGGAGGGAAGTAGG
$I_{e7}$	Left	CACTCTTTCAATAAATAGTGCTGG
	Right	AGTCCAGAGCACTAGATAAGAATG
$C_1$	Left	CCAAATTCATGGGGAGGGAACAC
	Right	CTGAGTGGAACCTGTCAATGCTG
$C_2$	Left	GAATGAGACAGCCAGATAAGGC
	Right	CTACCTTCAGCATCAGATCCAGG
$C_3$ (pair 1)	Left	CTTGCTATCCTCTGACCCCTGAG
	Right	GTAACATAAGGCAGGAGATATGG
$C_3$ (pair 2)	Left	CCTACGATCACTGGCCAGCATAAC
	Right	GGTTGACAGCATGGCAGAAACG

**Table S13** Primer sequences used in the PCR validation experiments of the insertions identified by OMSV from C666-1.

Module	Parameter	Estimation method/default value
Site	False positive rate ( $f_p$ )	1E-5, estimated by RefAligner
Site	False negative rate ( $f_n$ )	0.125, estimated by RefAligner
Site	P-value threshold	1E-9
Site, Size	Likelihood ratio threshold	1E-6
Site, Size	Minimum covering optical maps ( $M_{min}$ )	15 for Site, 10 for Size
Size	Minimum optical maps from each chromosome in heterozygous calls ( $k_{min}$ )	$\max(5, 0.4M)$ , where $M$ is the number of covering optical maps
Size	Global distance ratio location parameter ( $r_0$ )	1.0096, by MLE estimate of Matlab <code>fminsearch</code> function
Size	Global distance ratio scale parameter ( $\gamma$ )	0.0291, by MLE estimate of Matlab <code>fminsearch</code> function
Size	Minimum distance change ( $\delta$ )	$\max(2000, 0.05d_0)$ , where $d_0$ is the distance on the reference

**Table S14** Parameter values used in the SV detection modules of OMSV. Abbreviations of SV types: “Site” – extra/missing sites; “Size” – SVs with large size changes; “Complex” – complex SVs.

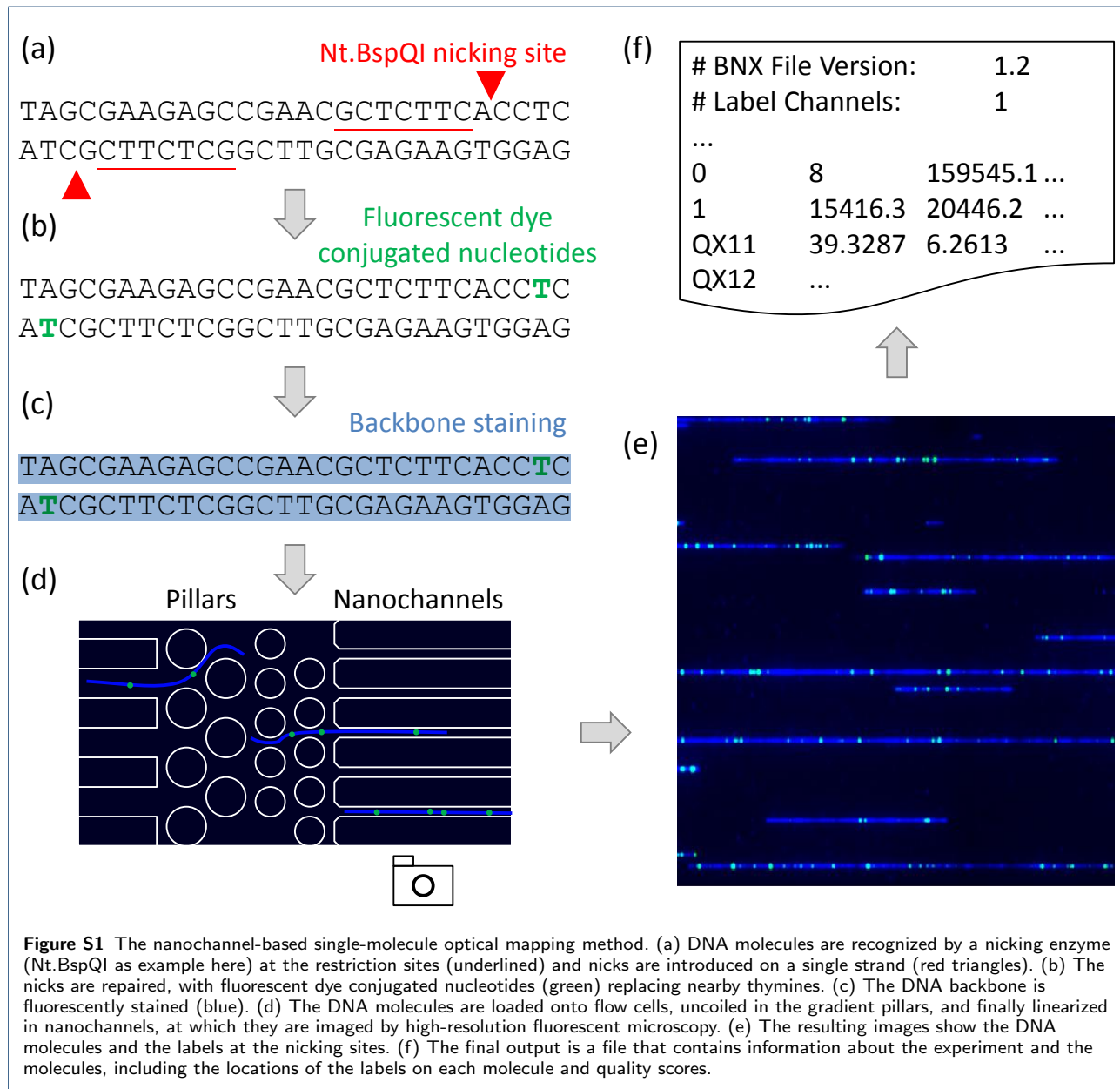
	SNP (The 1000 Genomes Project Consortium, 2010)	Indel (Lu et al., 2012)	Insertion/Deletion/Inversion (Pang et al., 2010)
Rate	1E-3	1E-4	1E-6
Number generated	2,910,896	298,715	2,942
Size range (bp)	1	2 – 70	5,000 – 100,000

**Table S15** Parameter values used in simulating a haploid genome (i.e., step 1 of simulation). The cited publications are the references for the chosen values.

Parameter	Symbol	Value used	Rationale
Number of optical maps	$n$	1,500,000	To get 100x coverage
Minimum DNA fragment size	$l_0$	100,000	Typical experimental protocol
Average DNA fragment extra size	$\mu_l$	100,000	Typical size in real data
Restriction enzyme		Nt.BspQI	Reasonable restriction site density
False negative rate	$f_-$	0.12	RefAligner's estimate from real data
False positive rate	$f_+$	1.2E-5	RefAligner's estimate from real data
Position parameter of sizing error	$o_\alpha$	1.00	Maximum likelihood estimate from real data
Scale parameter of sizing error	$s_\alpha$	0.02	Maximum likelihood estimate from real data
Imaging resolution	$d_{\frac{1}{2}}$	700	Observation from real data
Measurement error	$e$	50	Pixel resolution of optical map images

**Table S16** Parameter values used in generating simulated optical mapping data from a haploid genome (i.e., step 2 of simulation).

Supplementary figures



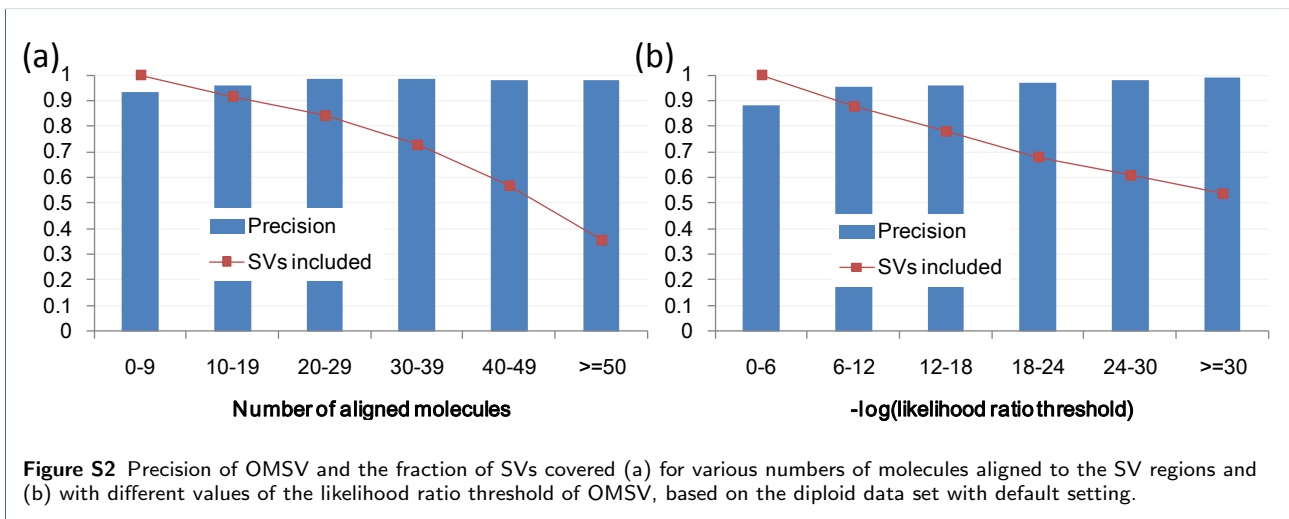


Figure S2 Precision of OMSV and the fraction of SVs covered (a) for various numbers of molecules aligned to the SV regions and (b) with different values of the likelihood ratio threshold of OMSV, based on the diploid data set with default setting.

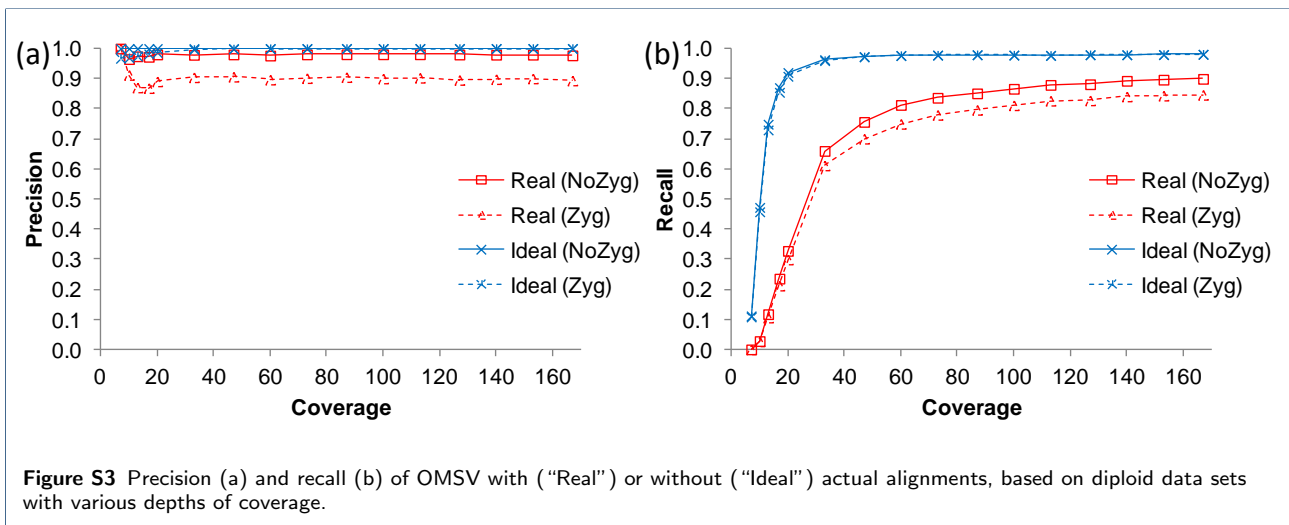


Figure S3 Precision (a) and recall (b) of OMSV with ("Real") or without ("Ideal") actual alignments, based on diploid data sets with various depths of coverage.

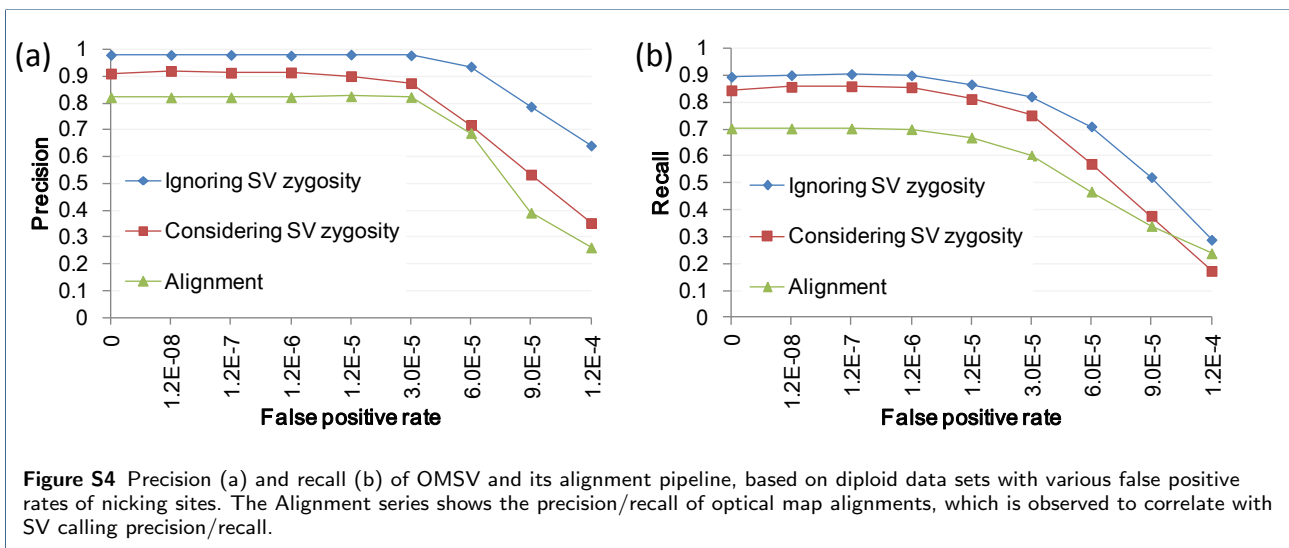
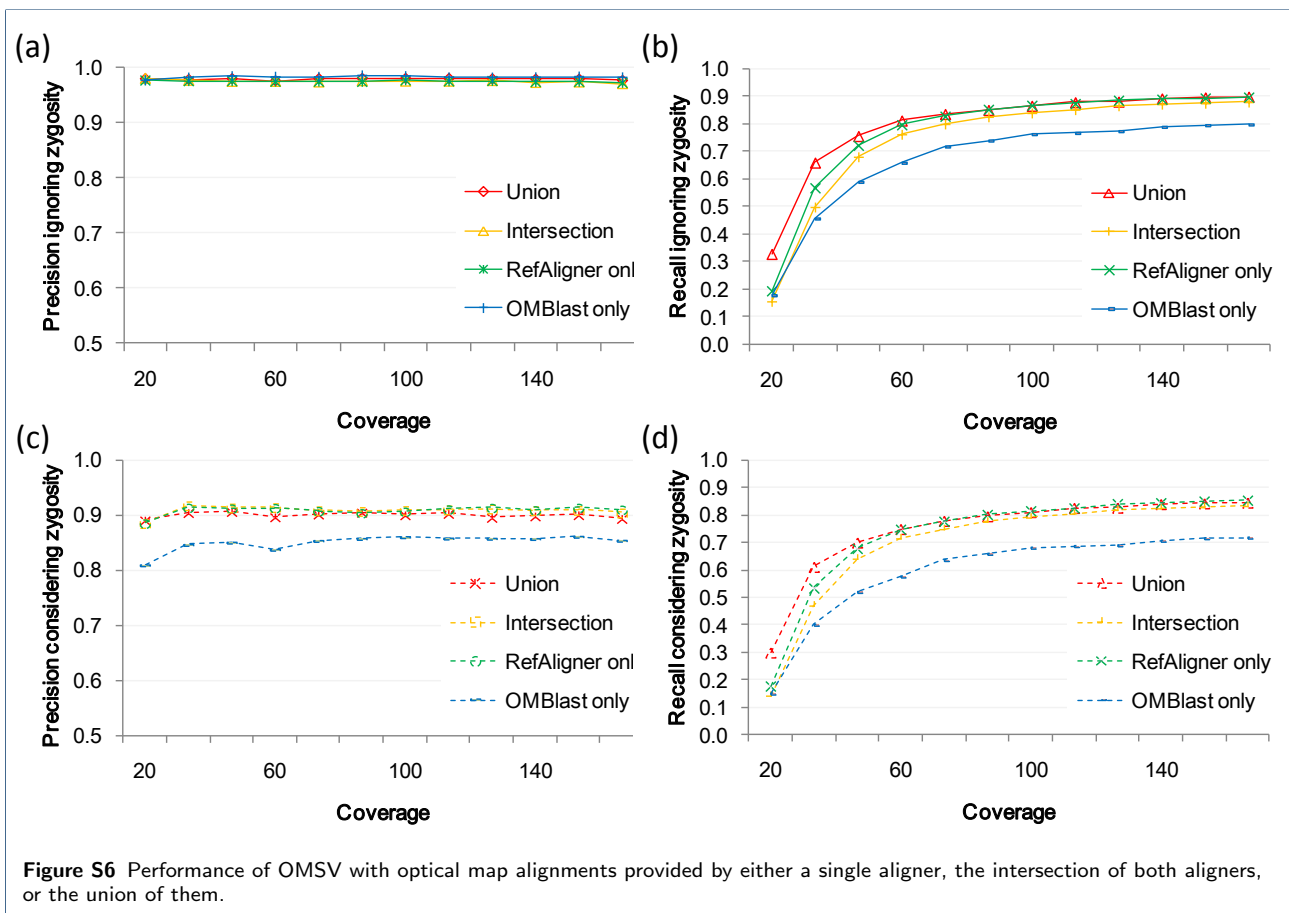
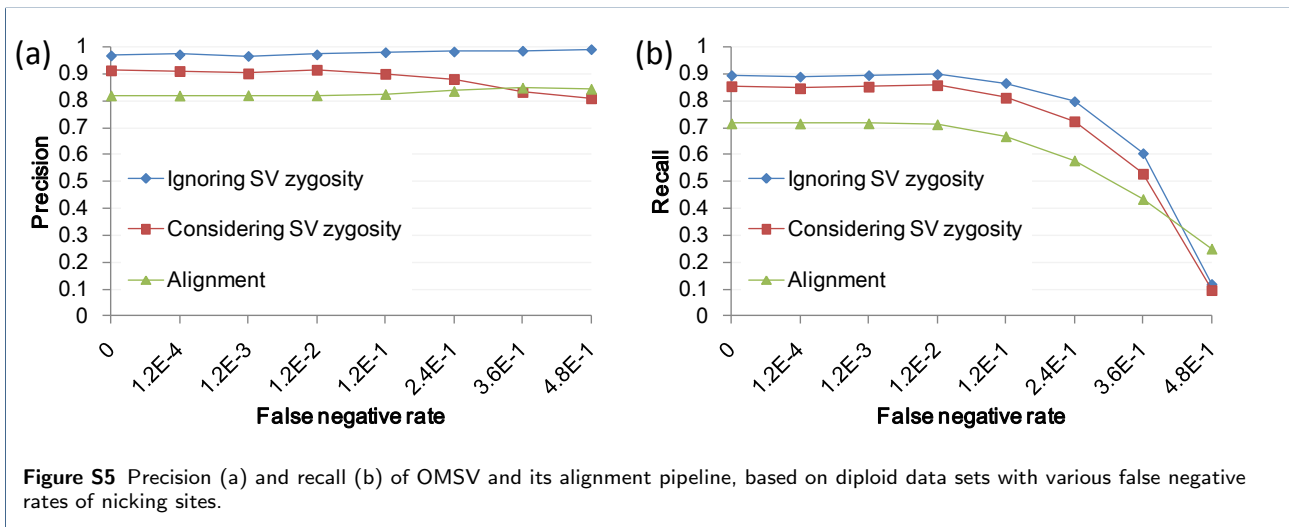
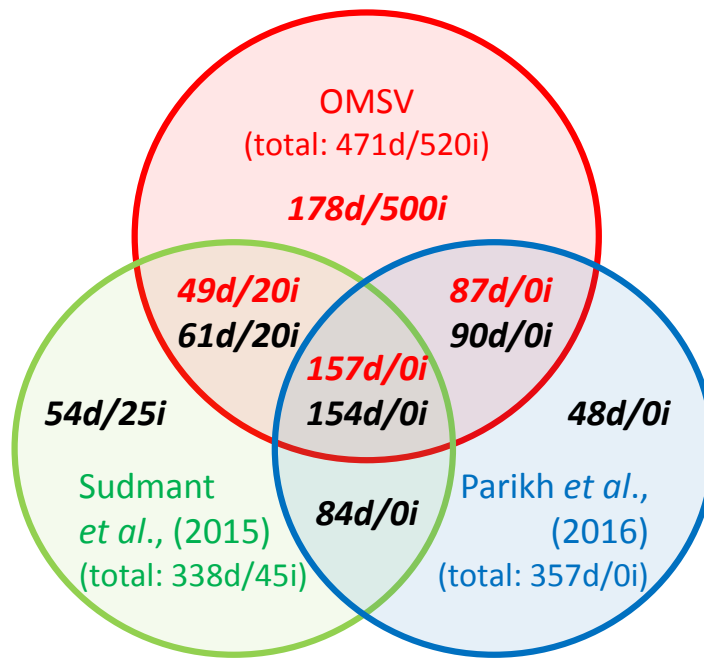
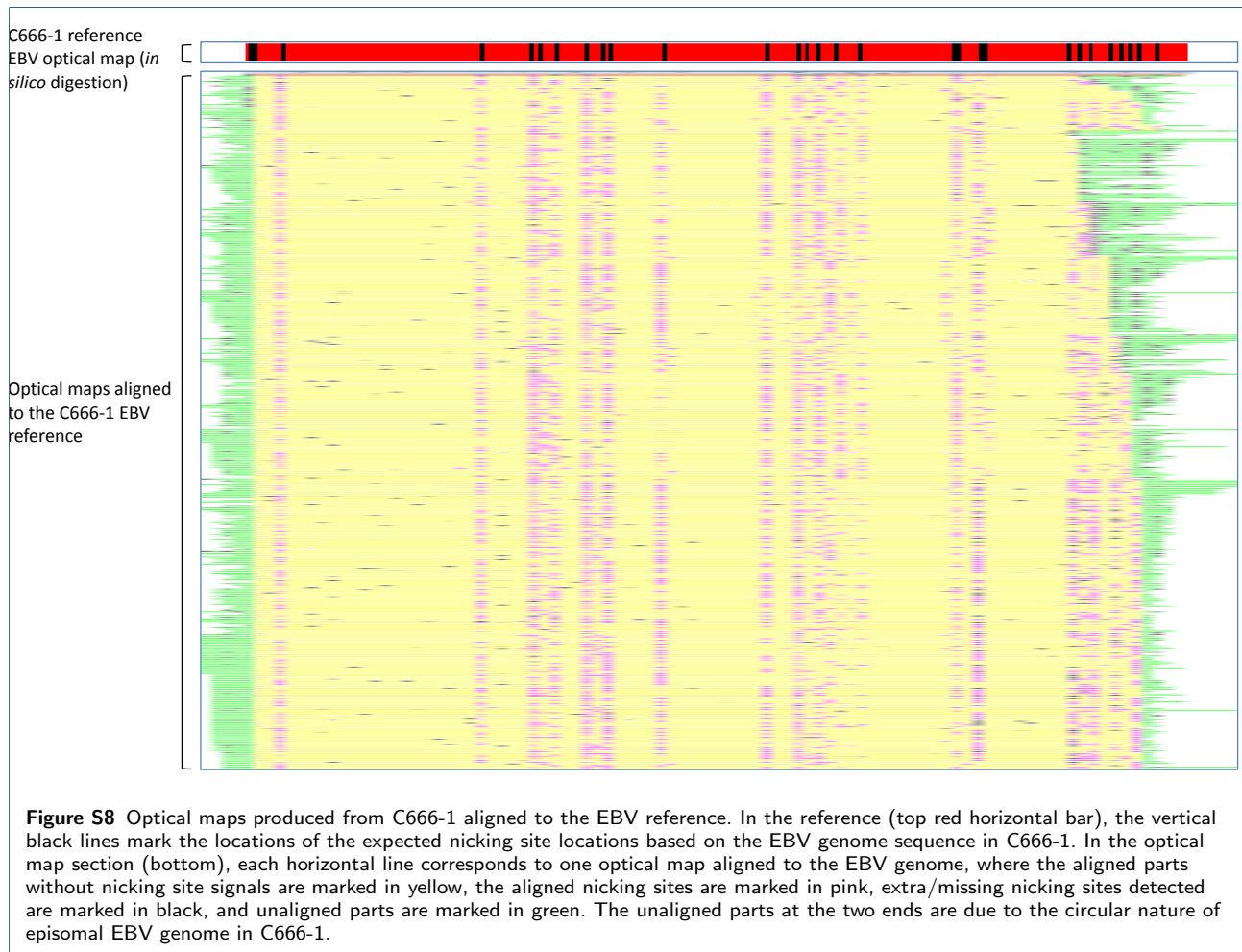


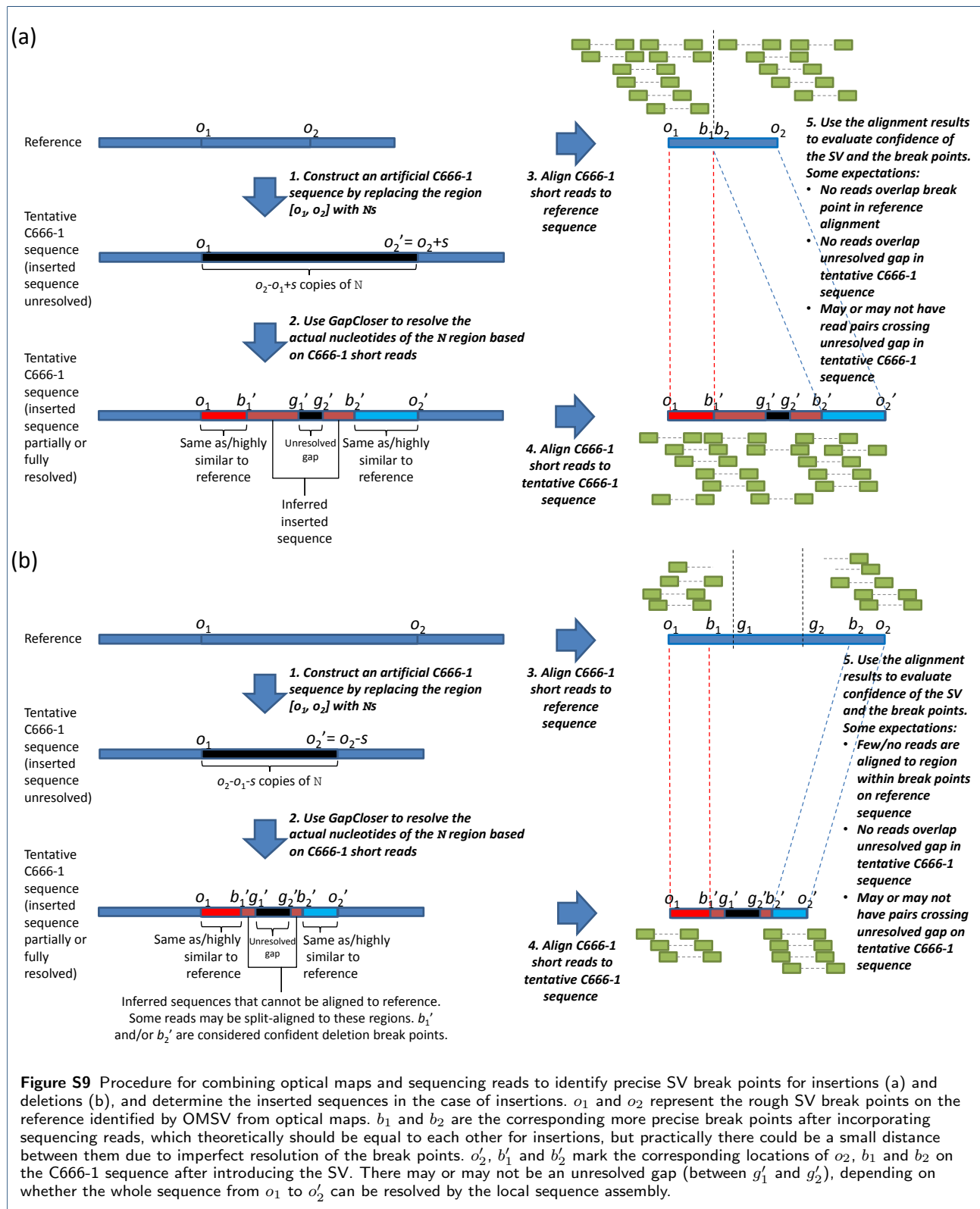
Figure S4 Precision (a) and recall (b) of OMSV and its alignment pipeline, based on diploid data sets with various false positive rates of nicking sites. The Alignment series shows the precision/recall of optical map alignments, which is observed to correlate with SV calling precision/recall.





**Figure S7** Comparison of indels detected by OMSV from NA12878 with two published lists obtained by sequencing-based methods. The SVs from the three individuals of the trio were integrated and de-duplicated, and then the ones contained in NA12878 were extracted from the resulting list. In each region, the numbers of deletions and insertions are shown as del/ins, where the numbers of indels identified by OMSV are in red while the numbers of indels reported in the previous studies are in black. Since an indel on one list could overlap multiple indels on another list, the red and black numbers in the same region are not necessarily the same. Loci with both an insertion and a deletion identified were not included in this comparison since the two published lists did not contain such cases.





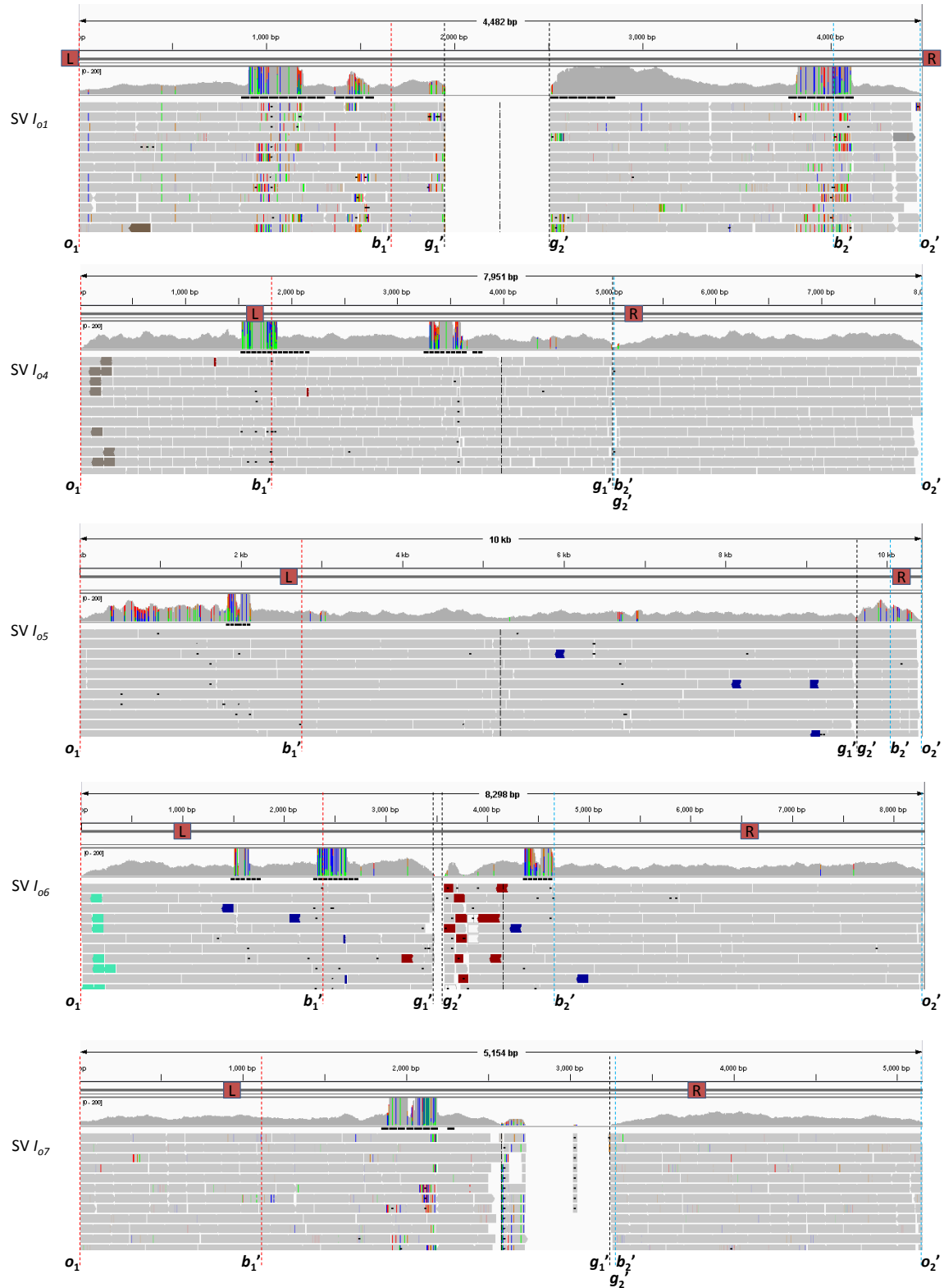


**Figure S10** Alignment of sequencing reads to the inferred C666-1 sequences of SVs  $I_{o1}, I_{o4}-I_{o7}$ . The L and R boxes mark the primer locations. Definitions of  $o_1, o_2', b_1', b_2', g_1'$  and  $g_2'$  are given in Figure S9. Sequencing read alignments are visualized by IGV. Some high-coverage regions with mismatches in the read alignments are repeat elements.

